Mineralium Deposita (2025) 60:697–721
https://doi.org/10.1007/s00126-024-01310-2

ARTICLE

# World-class amethyst-agate geodes from Los Catalanes, Northern Uruguay: genetic implications from fluid inclusions and stable isotopes

Fiorella Arduin-Rode[1] · Graciela Sosa[1] · Alfons van den Kerkhof[1] · Yves Krüger[2] · David Bajnai[1] · Andreas Pack[1] · Tommaso Di Rocco[1] · Pedro Oyhantçabal[3] · Klaus Wemmer[1] · Daniel Herwartz[4,5] · Swea Klipsch[4] · Bettina Wiegand[1] · Siegfried Siegesmund[1] · Mathias Hueck[1,5]

Received: 21 December 2023 / Accepted: 19 August 2024 / Published online: 23 September 2024


## Abstract

The amethyst and agate geodes from the Los Catalanes Gemmological District in Uruguay represent one of the main deposits of its kind worldwide. The geometry of the deposit is horizontal, with an irregular distribution of amethyst geodes within the upper level of the basalt lava flows and shows strong variations in their abundance, as well as quality, geometry, and shape. Reliable exploration guides are scarce, and the limited knowledge of the geological parameters controlling its occurrence makes exploration unpredictable, leading to inaccurate reserve estimation. Based on cutting-edge methods including nucleation-assisted microthermometry of one-phase fluid inclusions and determination of triple oxygen isotope in silicates and carbonates, as well as analysis of geode-hosted water and groundwater, we estimate the crystallisation temperatures in the range between 15 and 60 °C. These low temperatures point to amethyst crystallisation after the emplacement of the complete basalt pile. The mineralising fluid shows isotopic signatures consistent with meteoric water and very low salinities from pure water up to rarely over 3 wt% NaCl-eq., likely sourced from the groundwater hosted in the aquifers in the basaltic sequence and underlying units. Based on the insights provided by the new data, we propose the combination of open- and closed-system crystallisation inside pre-existing cavities due to the episodic infiltration of meteoric water in a rather stable geological context.

**Keywords** Amethyst geodes · Fluid inclusions · Isotope geochemistry · Triple oxygen isotopes · Los Catalanes Gemmological District · Paraná-Etendeka LIP

## Introduction

Amethyst, the violet variety of quartz, has been used as a gemstone for many centuries. Los Catalanes in northern Uruguay and Ametista do Sul in southern Brazil are the two major gemmological mining districts of this gemstone, and world leaders in the production of amethyst and agate geodes from basaltic lava. Amethyst has been mined for more than 150 years in the Los Catalanes Gemmological District, (Da Silva 1997; Techera et al. 2007; Baumann 2017), and in 2022 the deposit was listed as one of the "First 100 IUGS Geological Heritage Sites" (Hilario et al. 2022), highlighting the scientific importance and the natural value of the deposits. The limited knowledge on the geological controls of the mineralisation makes the localization of amethyst geodes unpredictable. Exploitation mainly relies on the miners' empirical experience,

Editorial handling: A. R. Cabral

✉ Fiorella Arduin-Rode
farduinrode@uni-goettingen.de

1 Geowissenschaftliches Zentrum, Georg–August–Universität Göttingen, Göttingen, Germany

2 Department of Earth Science, University of Bergen, Bergen, Norway

3 Instituto de Ciencias Geológicas, Facultad de Ciencias, Universidad de la República, Montevideo, Uruguay

4 Institute of Geology and Mineralogy, University of Cologne, Cologne, Germany

5 Institute for Geology, Mineralogy and Geophysics, Ruhr-University Bochum, Bochum, Germany

and reserve estimations are uncertain (Techera et al. 2007; Guerrero and Morales Demarco 2019).

Based on several studies on amethyst and agate deposits in Uruguay and southern Brazil during the last few decades, two contrasting interpretations have been advanced: Amethyst geodes were mineralised (1) by hot residual fluids, which were released from the cooling lava (Proust and Fontaine 2007b), or (2) by groundwater from the underlying aquifers, which are recharged by meteoric water (Juchem 1999; Gilg et al. 2003, 2014; Duarte et al. 2009; Morteani et al. 2010). These models reflect the main debates about the formation of the silica geodes more broadly, such as the source of the silica in solution and its hydrous transport, and the processes that control its final precipitation in the geodes, like changes in pH, silica oversaturation, and fluid rock-interaction (Iler 1979; Williams et al. 1985; Götze et al. 2020). Whereas a large range of temperatures have been proposed for the formation of amethyst and agate in basic volcanic rocks, recent contributions have indicated that this kind of mineralisation can take place at low temperatures (< 100 °C, e.g., Götze et al. 2020). This interpretation is based on the prevalence of one-phase aqueous fluid inclusions, which contain only one liquid phase at room temperature (Juchem 1999; Gilg et al. 2003; Duarte et al. 2009, 2011; Commin-Fischer et al. 2010; Morteani et al. 2010). On the other hand, bi-phase aqueous inclusions which contain liquid (L) and vapour (V) are rare. The quantitative systematics of one-phase aqueous fluid inclusions is technically complicated (Krüger et al. 2007), but in southern Brazil the crystallisation temperatures of amethyst geodes could be estimated in this way (Gilg et al. 2014). In addition to formation temperatures determined by fluid inclusions, also stable isotope data can provide formation temperatures by modelling the isotopic equilibrium achieved during mineral crystallisation. Stable isotope data acquired from amethyst, colourless quartz and chalcedony, support low formation temperatures of about 100 °C, or even less, and at least a partial participation of meteoric water during mineralisation (Juchem 1999). Recent advances in triple-oxygen-isotope systematics reveal significant advantages over traditional isotopic analyses because the influence of assumptions in modelling the isotopic signature of the initial water composition is reduced (Pack and Herwartz 2014).

In this paper, we present for the first time in Uruguay, a novel application of high-precision techniques, such as nucleation-assisted microthermometry of initial one-phase fluid inclusions and stable isotope studies, including the determination of triple oxygen isotopes, in combination with isotopic compositions of groundwater and geode-hosted water. The data presented in our study provide new insights regarding the formation of the Los Catalanes amethyst deposits, specifying the temperature crystallisation conditions of the amethyst, and the origin and evolution of the fluid involved in the amethyst mineralisation. Based on these observations, we propose an integrated model for the mineralisation that takes the regional geological setting into account.

## Geological context

The Paraná-Etendeka Large Igneous Province (PELIP, Fig. 1a,b) is the second largest igneous province worldwide. It covers a total area of approximately 1.2 million $km^2$ (Zalán et al. 1990) over at least six countries in South America (northern Uruguay, south-central Brazil, northern Argentina, eastern Paraguay), and in Africa (Namibia and Angola). The estimated volume of the magmatic sequence is of approximately 1.7 million $km^3$ (e.g., Frank et al. 2009), reaching thickness of 1,700 m in its depocenter (Cordani and Vandoros 1967; Zalán et al. 1990; Peate 1997). Together with the Parana Basin, it overlies a complex collage of Precambrian crustal blocks (Zalán et al. 1990), comprising Archean to Proterozoic units tectonically juxtaposed in the late Neoproterozoic assembly of Gondwana, during the Brasiliano-Pan African Orogenic Cycle (e.g., Oyhantçabal et al. 2011, 2018; de Brito Neves and Fuck 2013; Hueck et al. 2022). It represents a short-lived magmatic event preceding the break-up of Gondwana and the opening of the South Atlantic Ocean in the Lower Cretaceous, between 135 and 132 Ma (e.g., de Assis et al. 2011; Florisbal et al. 2014; Rocha et al. 2020, 2023). Aeolian sandstones deposited in an arid environment underly the basaltic pile and form irregular layers of up to some meters intercalated between the lava flows (Peate 1997). The PELIP comprises mainly tholeiitic basalt and basaltic-andesites (97.5%) with subordinated acid lavas (2.5%) (Bellieni et al. 1984) and can be divided into two major units regarding their first-order chemical signature, with a predominance of high-Ti rocks (2–4 wt.% $TiO_2$) in the north and low-Ti lavas (< 2 wt.% $TiO_2$) in the south (Bellieni et al. 1984; Mantovani et al. 1985; Peate 1997). Peate et al. (1992) proposed the migration of volcanic activity from the south to the northwest. Six magma types have been distinguished based on major- and trace- element abundance and ratios (Peate et al. 1992): two low-Ti types (Gramado, Esmeralda), and four high-Ti types (Urubici, Pitanga, Paranapanema, Ribeira). The regional distribution of distinct high-Ti and low-Ti magma types implies that magma generation occurred over a wide area and involved different mantle sources (e.g., Peate 1997). The deposition of the volcano-sedimentary sequence is largely controlled by the reactivation of first-order regional structures (e.g., Rostirola et al. 2000; Holz et al. 2006; Strugale et al. 2007; Hueck et al. 2017, 2020; Veroslavsky et al. 2021; Morales et al. 2021).

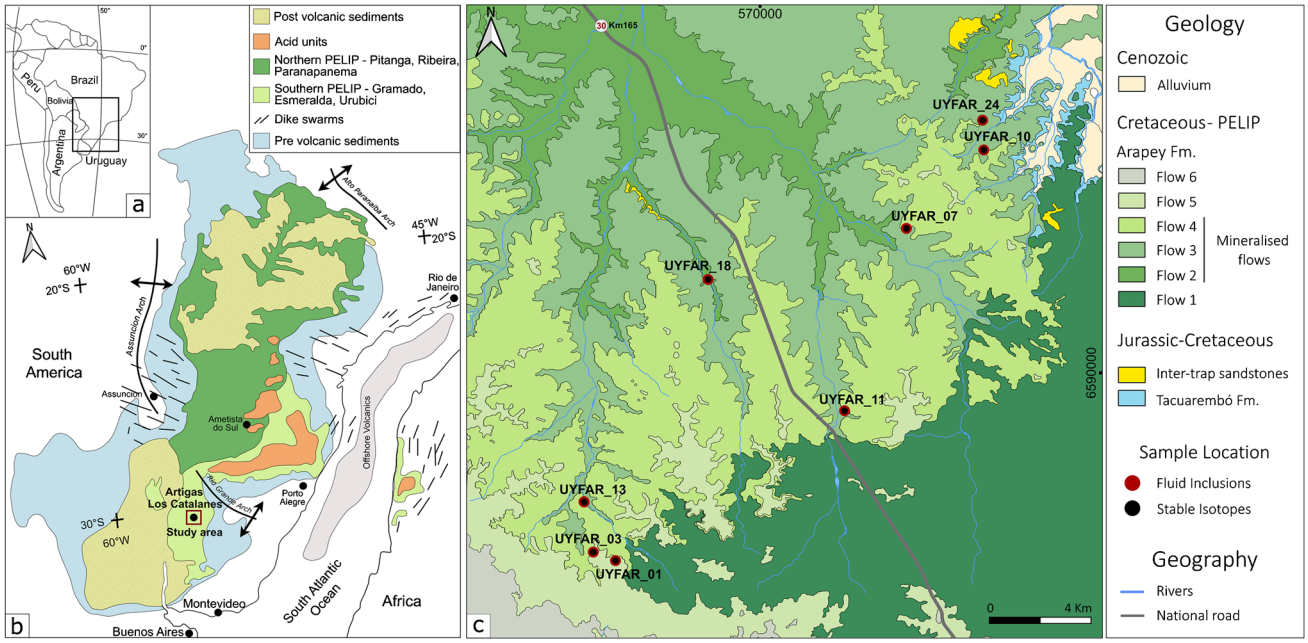


**Fig. 1** Geological context and study-area localisation. **a** Location of the Paraná Basin in South America. **b** Schematic geological map of the Paraná-Etendeka Large Igneous Province (PELIP) in South America and Africa in a pre-drift reconstruction (after Rossetti et al. 2018). **c** Geological map of the Los Catalanes Gemmological District, Artigas, northern Uruguay (after Techera et al. 2007). Coordinates in C are presented in the UTM projection (Zone 21S, Datum WGS84)

The stratigraphic unit assigned to the lavas of the PELIP has different denominations depending on the country in which they are described. The main unit comprising the lavas is known as the Arapey Formation in Uruguay, the Serra Geral Formation in Brazil, the Alto Paraná Formation in Paraguay, and the Posadas Member and Curuzú Cuatiá Formation in Argentina. Equally, the underlying sandstone units also have different country-specific names, which in Uruguay correspond to the Tacuarembó and Rivera Formations, and in Brazil to the Botucatú and Pirambóia Formations. In this work, we follow the Uruguayan conventions, i.e., the Arapey Formation refers to the basalt and the Tacuarembó and Rivera Formations to the underlying sandstone.

## Geology of the mining area – Los Catalanes Gemmological District

The Los Catalanes mining district (Fig. 1c) is located 60 km south of the city of Artigas in northern Uruguay, close to the international border with Brazil. The geology of the mining district is dominated by volcanic rocks underlain by sandstones, which also occur as inter-trap deposits between single volcanic flows and as xenoliths. Geological mapping of the region identified six units corresponding to different lava flows (Techera et al. 2007), three of which host amethyst geodes. The flows are low-Ti Gramado-type lavas (Hartmann et al. 2010). The basal Flow 1 covers a large extension in the south-southeast of the study-area. The rocks are characterised by a meter-scale banded alternation of dark aphanitic basalt with magmatic flow structures and a reddish basaltic volcanic breccia. Flows 2 to 6 present horizontal dispositions with a gentle dip to the north (~3°), in which Flow 2 (Mata Olho, Hartmann et al. 2010) is characterised by pahoehoe basalt lavas, Flow 3 (Catalán, Techera et al. 2007) by aa andesite lavas, Flow 4 (Cordillera, Techera et al. 2007) comprise pahoehoe basaltic andesite lavas, Flow 5 is dominated by aa basaltic andesite lavas, and Flow 6 comprises basaltic andesite (Hartmann et al. 2010). The thickness of the individual flows never exceeds 60 m. Locally, breccias with sand matrix and sandstone with aeolian structures are found along the contact between lava flows (Techera et al. 2007).

Amethyst and agate geodes are hosted in the upper levels of Flows 2 (Mata Olho), 3 (Catalán), and 4 (Cordillera). The mineralised levels are subhorizontal, up to 5 – 9 m thick (Fig. 2a), with strong lateral variation in the concentration and size of the geodes. The mineralised levels differ from each other in terms of shape, size, and amount of the geodes. Flow 3 (Catalan) hosts most of the mining prospects due to the quality and concentration of its geodes. This is the most productive and the thickest flow, reaching exceptionally up to 8–9 m and hosting mineralised geodes with dimensions up to 5 m in length and reaching the order of 10 tons in weight. The geodes

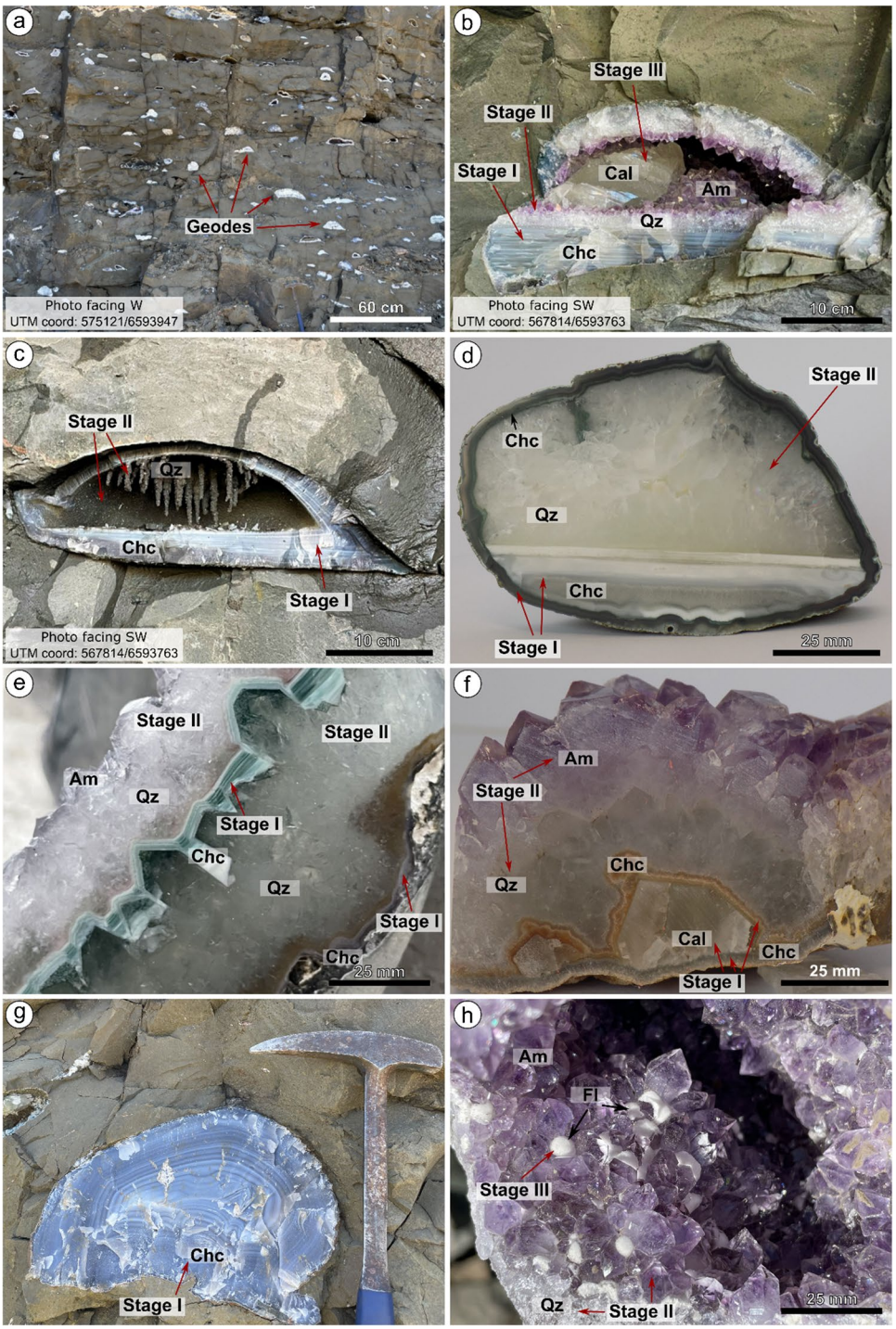


**Fig. 2** Photographs of geodes. **a** Open-pit mine wall, note the horizontal disposition of the geodes within the mineralised level. **b** Agate-amethyst-calcite geode, from the rim to the core of the geode: host basalt, chalcedony, horizontal banded chalcedony, colourless quartz, amethyst, late calcite (stage I, II and III). **c** Agate (chalcedony) geode in situ with quartz stalactites (stages I and II). **d** Chalcedony, horizontal banded agate and colourless quartz geode (stages I and II). **e** Detail of different mineral associations in geode with repeated crystallisation sequence. From the rim to the core (right to left): chalcedony (stage I), colourless quartz (stage II), banded chalcedony (stage I), colourless quartz and amethyst (stage II). **f** Detail of chalcedony and early calcite (stage I), colourless quartz and amethyst (stage II), rim of the geode down and core up. **g** Detail of banded agate geode in situ (crystallisation stage I). **h** Detail of amethyst (stage II) geode, overgrown by spherulites of white fluorite (stage III)

include irregular, spherical, oblate and prolate shapes mainly with horizontal long axes. Flow 2 (Mata Olho) is the second most productive, hosting mostly prolate elliptical geodes with horizontal long axes that typically do not exceed 50 to 70 cm and 100 kg. Flow 4 (Cordillera) hosts a high concentration of cm- to meter-scale geodes and vesicles. This flow is the less exploited of the three, and its geodes show mostly cylindrical shapes with planar bases and vertical long axes as long as two meters, and

exceptionally, three meters (locally called “capillas”, which is the Spanish word for chapels).

## Mineral phases and petrography of the geodes

The mineral phases in the geodes are similar in the three mineralised lava flows with concentric crystallisation from the rim to the core (Fig. 2b-h), in some cases presenting siliceous stalactites (Fig. 2c) which evidence the presence of microfractures. Different stages were defined according to the spatial and temporal relation between the different minerals (Fig. 3).

Stage I minerals in contact with the host basalt are present in all the geodes and always precede the amethyst (pre-amethyst). At the contact with the basalt, a mm-thick rim of green fibrous celadonite, in association with zeolite (Fig. 4a) and smectite is normally present. Repeated concentric layers of fibrous chalcedony with radial distribution and often forming spherulites typically constitute the outer rim (Fig. 4b, c). Sometimes brownish spherulites of amorphous opal (identified by Raman) are present at the contact with the basalt. Chalcedony is the most abundant mineral of stage I, sometimes surrounding euhedral, mm- to cm-scale calcite crystals (Figs. 2f, 4d), and grading into mm-scale coarse-grained colourless quartz. Sub-mm-scale patches of green, fibrous to colloform celadonite, magnetite-ilmenite exsolutions and scarce pyrite are sometimes present as intergrowths in the interstices of chalcedony layers, which may affect the macroscopic colour of the mineral assemblage of stage I (Fig. 4e). Stage II (syn-amethyst) and stage III (post-amethyst) vary in dimension or even do not develop. Therefore, many geodes contain almost only chalcedony (stage I) (Fig. 2g). The transition from stage I to II is characterised by the gradation of chalcedony into coarse-grained colourless quartz (Fig.s 2b, e, f, 4c–f). Stage II presents mm-scale anhedral coarse-grained colourless quartz, progressively increasing in size towards the central cavity of the geode, resulting in idiomorphic amethyst or colourless quartz crystals (Figs. 2e, f; 4c, d). Occasionally, prasiolite (green quartz) can be observed within the colourless quartz sequence. The transition between colourless quartz and amethyst may be gradual within the same crystal or marked by the formation of a new single amethyst crystal (Fig. 2f). Development of Brazilian twining (Fig. 5a, b) and microstructures formed in response to growth tension, such as undulose extinction, subgrains, lamellae and sets of braided sigmoidal microfractures parallel to the c-axis (Fig. 5c) have been observed in restricted zones of individual crystals, mostly associated to competitive growth leading to coarse-grained colourless quartz. Inclusions of tabular brownish hematite are often present in the amethyst crystals. In some geodes, stage II is followed by the subsequent growth of stage I minerals, resulting in alternations between both stages

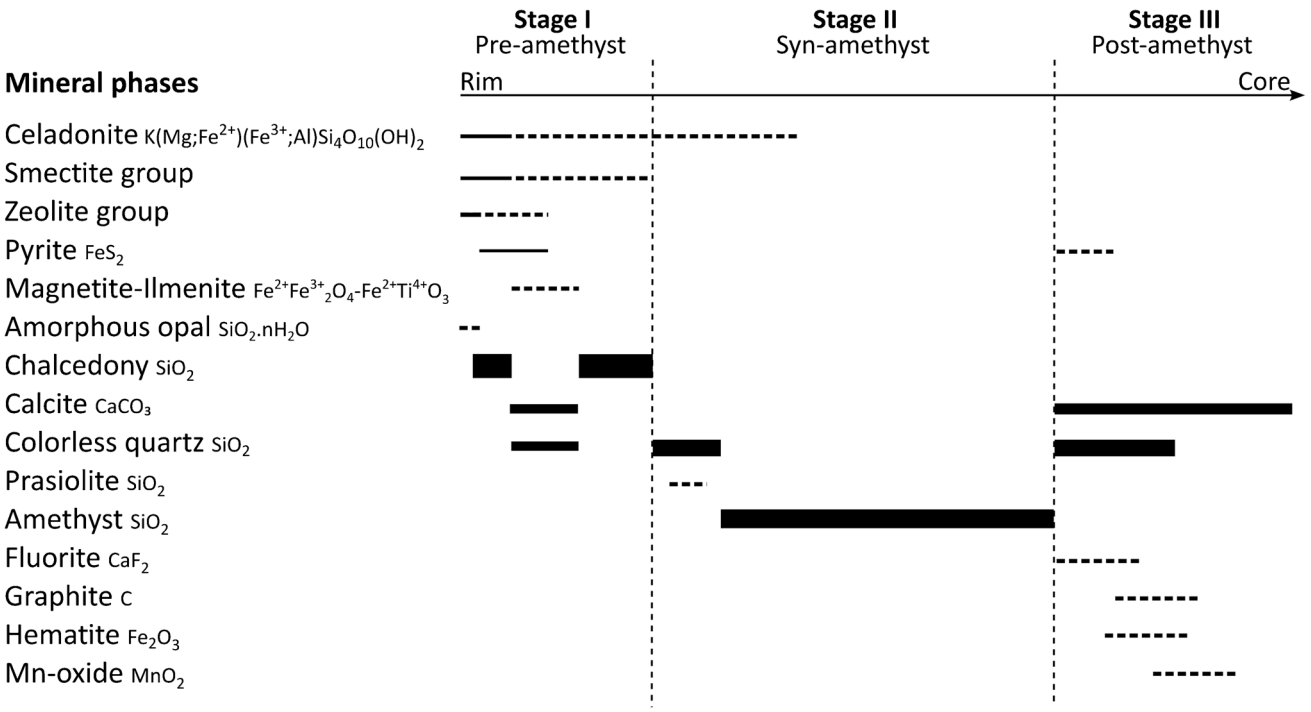


**Fig. 3** Crystallisation sequence of geodes. Line thickness indicates relative abundance

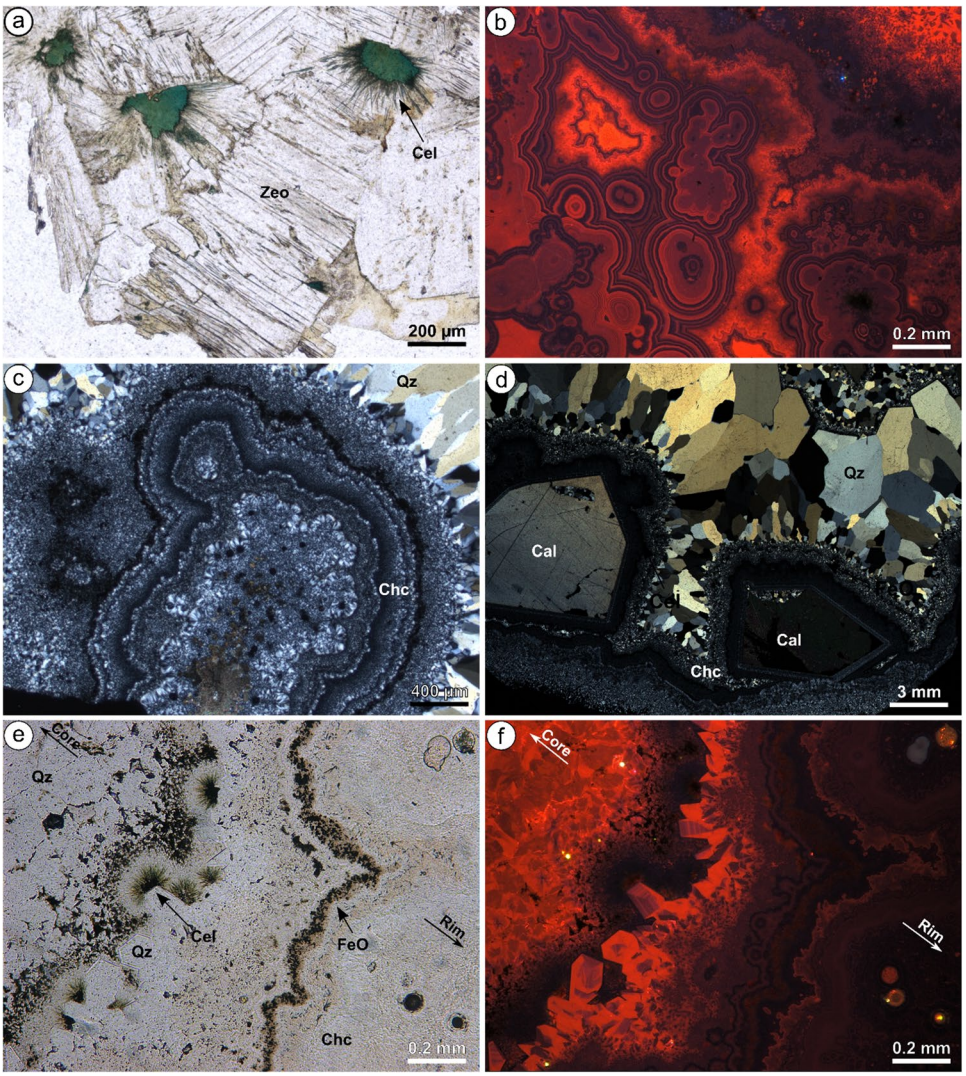


**Fig. 4** Photomicrographs showing petrographic features of the geodes (stages I and II) in polarised-light and cathodoluminescence (CL) microscopy. Abbreviation names of minerals according to Whitney and Evans (2010). **a** Intergrowth of zeolite and celadonite (stage I). **b** Chalcedony under CL, highlighting concentric growth patterns that are not distinguishable in conventional microscopy (stage I). **c** Repeated bands of chalcedony (stage I) transitioning to macro-crystalline quartz (stage II), cross-polarised light. **d** Transition of chalcedony and early calcite (stage I) to coarse-grained colourless quartz and amethyst (stage II), cross-polarised light. **e** Repeated transition of stage I to stage II, resulting in a banded fabric of alternating chalcedony and coarse-grained colourless quartz layers. Note the thin layers of celadonite and Fe-oxides, which gives the macroscopic colour to the chalcedony. **f** Same as e under CL, highlighting the banded fabric. Images a to d are positioned with the rim of the geode down and the core up

(Figs. 2e, 4e, f). Crystallisation stage III is represented by mm- to dm-scale calcite crystals with a large variety of morphologies (e.g., Fig. 2b). Under the microscope, calcite crystals show different habits and microstructures, from perfectly euhedral, homogeneous transparent crystals to light yellow smoky anhedral crystals with deformation microstructures, such as undulose extinction and subgrains (Fig. 5d, e, f). In some cases, euhedral crystals of pyrite are present along microfractures in late calcite crystals or on top of stage II minerals. Occasionally acicular mm-size goethite, tabular hematite, graphite and white mm-size fluorite spherulites (identified by Raman microscopy) constitute the last mineral phase (Fig. 2h).

## Samples

Detailed geological surveys of the Los Catalanes Gemmological District were carried out in more than thirty active open-pit and underground mines. Geological observations and sampling were also carried out in natural outcrops in the surrounding areas. Collected samples comprise the three mineralised flows (Mata Olho, Catalán, Cordillera) and the different mineral crystallisation stages of the geodes. In addition, three samples of geode-hosted water and three samples of groundwater from surrounding boreholes were collected. The most representative samples were studied in detail and are summarized in Table 1.

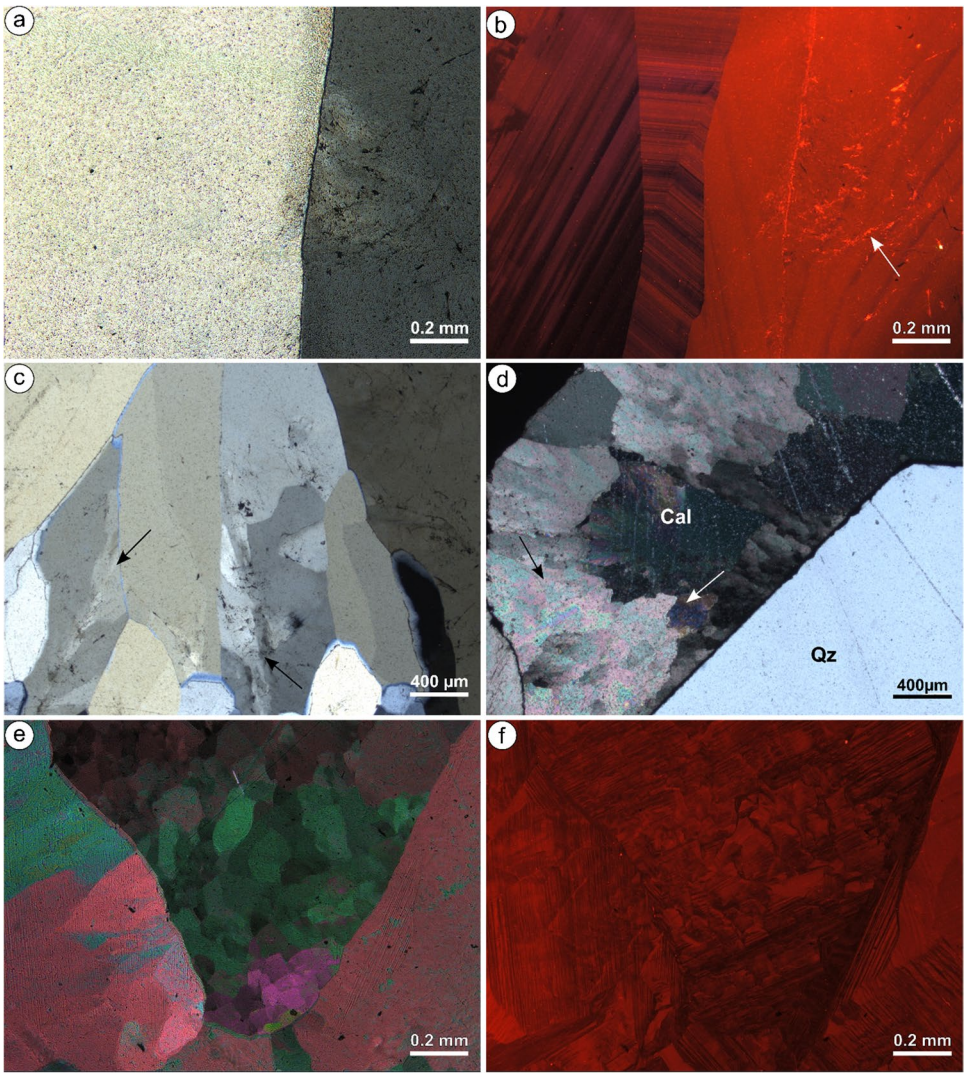


**Fig. 5** Photomicrographs of petrographic features of geodes (stages II and III) in polarised-light and cathodoluminescence (CL) microscopy. Abbreviation of mineral names is according to Whitney and Evans (2010). **a** Undeformed amethyst crystal (left) in contact with a deformed one, characterised by the presence of undulose extinction (right), cross-polarised light. **b** Same as a under CL, highlighting undisturbed crystal-growth zoning and twining in the undeformed crystal (left) and deformation microstructures, such as healed microfractures (indicated by arrows), in the deformed one (right). **c** Amethyst crystals (stage II), locally displaying deformational microstructures, such as undulose extinction (indicated by arrows), cross-polarised light. **d** Sharp contact between amethyst (stage II) to late calcite (stage III). Note the undulose extinction and subgrains in calcite (indicated by arrows), cross-polarised light. **e** Late calcite (stage III) displaying deformation microstructures, such as undulose extinction and subgrains, cross-polarised. **f** Same as e under CL, highlighting cleavage and growth zones. All images are positioned with the rim of the geode down and the core up

**Table 1** Localisation of the studied samples. Coordinates are presented in the UTM grid, zone 21S and datum WGS84. Abbreviation of mineral names is according to Whitney and Evans (2010)

| Sample | Sample id | Flow | Mineral phases | Stages | Coord UTM | |
|---|---|---|---|---|---|---|
| Geode minerals | UYFAR-01 | 4 | Cel + Chc + Qz + Am | I, II, III | 564486 | 6582633 |
| | UYFAR-03 | 4 | Qz + Am | II | 563638 | 6582996 |
| | UYFAR-11 | 3 | Cel + Chc + Cal + Qz + Cal | I, II, III | 573194 | 6588384 |
| | UYFAR-13 | 3 | Cel + Chc + Qz | I, II | 562930 | 6585120 |
| | UYFAR-10 | 3 | Cel + Chc + Qz + Am + Cal | I, II, III | 578518 | 6598509 |
| | UYFAR-24 | 3 | Cel + Chc + Cal | I, III | 578021 | 6598849 |
| | UYFAR-07 | 2 | Cel + Chc + Qz + Am + Cal | I, II, III | 575576 | 6595370 |
| | UYFAR-18 | 2 | Cel + Chc + Cal + Chc + Qz + Am | I, II, III | 567832 | 6593401 |
| Geode water | UYFAR-10 | 3 | Opened geode | I, II, III | 578518 | 6598509 |
| | UYFAR-11 | 3 | Closed geode | I, II | 573194 | 6588384 |
| | UYFAR-11–2 | 3 | Closed geode | I, II, III | 573194 | 6588384 |
| Groundwater | UYFAR-LeStage | | Well in basalt 60 m depth | | 573373 | 6596304 |
| | UYFAR-CPlat | | Well in basalt 40 m depth | | 554349 | 6625833 |
| | UYFAR-PÑang | | Well in basalt 40 m depth | | 587099 | 6492063 |

## Analytical methods

### Cathodoluminescence microscopy

Polarised-light and cathodoluminescence (CL) microscopy was performed at the Geoscience Centre of the University of Göttingen. Doubly polished thin sections were carbon-coated and studied with optical cathodoluminescence microscopy (O-CL) using a hot cathode HC3-LM-Simon-Neuser CL microscope (Neuser et al. 1995), equipped with a Kappa DX 40C Peltier-cooled camera. The operating conditions were acceleration voltage of 14 kV and a beam current of < 1 mA, corresponding to a beam current density of 20–40 µA $mm^{-2}$.

### Fluid inclusion studies

Fluid inclusions were analysed on doubly-polished plates of 150 – 200 µm thickness, which were prepared from the mirror side of the sections used for CL microscopy. One-phase liquid inclusions were analysed at the Department of Earth Science, University of Bergen, using nucleation-assisted microthermometry (Krüger et al. 2007). This technique has been applied in studies focusing on low-temperature minerals such as calcite, gypsum, quartz-amethyst and halite, particularly those formed under near-subsurface conditions (e.g. Krüger et al. 2011, 2013; Gilg et al. 2014; Løland et al. 2022; Koltai et al. 2024; Arnuk et al. 2024). The setup used for the measurements consists of a Ti:Sapphire femtosecond laser (CPA 2101, Clark-MXR) and a Olympus BX53 microscope, equipped with a Linkam THMSG-600 heating-freezing stage and a digital camera (pco.edge 3.1). The laser that provides ultra-short laser pulses at a wavelength of 775 nm is coupled into the microscope light path via a dichroic short-pass filter (675DCSPXR, Omega optical), focussed on the fluid inclusions through a 100 × long working distance objective (Olympus LMPLFLN). Temperature calibration of the heating-freezing stage was performed with synthetic fluid inclusions using the eutectic temperature of the $H_2O$ – NaCl system at -21.2 °C, the triple point of pure water at 0 °C and the critical temperature of $CO_2$ in the $H_2O$ – $CO_2$ system at 31.4 °C. Temperature reproducibility (precision and accuracy) is estimated at ± 0.1 °C between -30 and + 40 °C, and ± 0.2 °C between 40 and 120 °C. The setup allows stimulating vapour bubble nucleation in metastable liquid inclusions by means of single ultra-short laser pulses under simultaneous visual observation and subsequent microthermometric measurements. Once the vapour bubble formed, total homogenization (Tht) was measured upon subsequent heating (L + V → L). This temperature represents the minimum trapping temperature of the fluid. In addition, total retrograde homogenization temperatures ($Tht_r$) could be measured upon cooling (L + V → L) in inclusions with prograde Tht below 55 °C. Finally, ice-melting temperatures (Tm-ice) were measured under equilibrium conditions – i.e., in the presence of vapor bubble (ice + L + V → L + V). This temperature was used to calculate the salinity of the fluid. For calcite-confined inclusions, this is no issue because of the volume increase of inclusions induced by ice nucleation, which generally results in spontaneous vapor bubble nucleation. For inclusions in quartz and amethyst that withstand much higher internal pressure, in contrast, vapor bubble nucleation had to be stimulated. The stimulation was triggered some tenths of a degree below the expected ice melting temperature to achieve equilibrium conditions for Tm-ice measurements (ice + L → ice + L + V). We note that ice-melting temperatures were measured at the very end of the analytical procedure, following completion of Tht and Thr measurements.

Bi-phase (liquid – vapor) fluid inclusions at room temperature were studied at the Geoscience Centre of the University of Göttingen. Phase transitions were investigated using a Linkam THMSG-600 heating-freezing stage, cooled with liquid nitrogen (Shepherd 1981). Calibration was performed with synthetic fluid-inclusion standards. The accuracy is better than ± 0.5 °C between -56.6 °C (melting point of $CO_2$) and 0 °C, while for temperatures between 50 and 300 °C, it is better than ± 2 °C. Salinity in the $H_2O$ – NaCl system was calculated from the revised equations of Bodnar (2003).

### Stable isotopes

Triple oxygen and carbon isotope compositions of silicates and carbonates were determined at the Geoscience Centre of the University of Göttingen. Measurements of triple oxygen isotopes in chalcedony, colourless quartz, and amethyst were performed by IR-Laser fluorination using $BrF_5$ as a reagent (Sharp 1990). The extracted $O_2$ was cleaned from contaminant gases using cryogenic traps, held at liquid-nitrogen temperature, a 5-Å-mesh molecular sieve trap, and a gas chromatograph. After purification, sample $O_2$ was transferred, via He stream at 10 mL $min^{-1}$, into a second molecular sieve trap located in front of a Thermo 253Plus mass spectrometer. After pumping He out of this trap, sample $O_2$ was expanded at 50 °C into the bellows of the mass spectrometer (Pack et al. 2016). Samples were measured relative to a reference gas calibrated using $O_2$ released from San Carlos olivine ($\delta^{18}O = 5.23‰$, $\Delta'^{17}O_{0.528} = -52$ ppm; see Pack 2021). Measured oxygen isotope ratios are expressed in the delta notation ($\delta^{17}O$, $\delta^{18}O$) relative to the Vienna Standard Mean Ocean Water (VSMOW). For mass-dependent processes, variations in $\delta^{17}O$ are about half of variations in $\delta^{18}O$. Deviations from such predicted relationship are expressed using the $\Delta'^{17}O$ notation, where:

$$\Delta'^{17}O = 1000 \cdot \ln\left(\frac{\delta^{17}O}{1000} + 1\right) - 0.528 \cdot 1000 \cdot \ln\left(\frac{\delta^{18}O}{1000} + 1\right)$$

Based on replicate analyses of San Carlos Olivine, the analytical uncertainty in $\delta^{18}O$ and $\Delta'^{17}O$ were ~ 0.2‰ and ~ 7 ppm (1σ), respectively. Laser fluorination, gas purification, gas transfer, and measurement protocol were automatized using LabVIEW to avoid any user-specific effects. Further details on the analytical procedure are given in Pack et al. (2016) and Peters et al. (2020).

The triple oxygen isotope composition of calcite was measured using tunable infrared laser direct absorption spectroscopy (TILDAS; Aerodyne, USA), combined with a custom gas inlet system (Bajnai et al. 2023). Acid digestion of carbonates was performed offline. Approximately 2 mg of calcite and 2 $cm^3$ 103% phosphoric acid were loaded into McCrea-style glass reaction vessels (McCrea 1950). The vessels were placed in a water bath held at a constant temperature of 25 °C, and the reaction was left to develop overnight. The resulting gas was dried and purified using a cryogenic trap before being transferred to the TILDAS. To scale the measured "raw" $\Delta'^{17}O$ and $\delta^{18}O$ values, we used our in-house light and heavy $CO_2$ gases. These gases were scaled to NBS-18 and IAEA-603 (Wostbrock et al. 2020a), as described in Bajnai et al. (2024).

In addition to the TILDAS measurements, the $\delta^{13}C$ and $\delta^{18}O$ values of carbonates were determined using isotope-ratio mass spectrometry. Approximately 0.08 mg of calcite was reacted with approximately 103% phosphoric acid using a Thermo KIEL IV carbonate device, connected to a Thermo Delta Plus mass spectrometer. The $\delta^{13}C$ values are reported on the VPDB scale and the $\delta^{18}O$ values on the VSMOW scale based on international standards (IAEA-603 and NBS-18), measured along with the samples.

Measurements of triple oxygen isotopes of geode-hosted and groundwater from boreholes were performed at the Institute of Geology and Mineralogy at the University of Cologne, following the method by Baker et al. (2002), optimized by Barkan and Luz (2005), and Surma et al. (2015). Internal laboratory standard waters were calibrated against VSMOW-2/SLAP-2 (Standard Light Antarctic Precipitation), following the SMOW-SLAP calibration procedure (Schoenemann et al. 2013). At least two laboratory standards were analysed together with the unknowns in every analytical session, being all data reported on SMOW-SLAP scale (Herwartz et al. 2017). The long-term reproducibility (1σ standard deviation) of measurements is 0.25‰ for $\delta^{18}O$, and 0.009‰ (9 per meg) for $\Delta'^{17}O$.

Measurements of $\delta^{2}H$ and $\delta^{18}O$ in geode-hosted water and groundwater from surrounding boreholes were performed at the Geoscience Centre of the University of Göttingen. Values of $\delta^{18}O$ and $\delta^{2}H$ (in ‰) were determined using a liquid–water isotope analyser (LGR, IWA-35-EP), and the VSMOW as the reference material. The average precision of the measurements is ± 0.2‰ (Hamdan et al. 2016).

### Hydrogeochemistry

The same samples analysed for triple oxygen isotopes and deuterium were also measured for anion and cation compositions at the Laboratory of the Physical Geography Department (Georg-August-Universität Göttingen). Total concentrations of Na, Mg, K, Ca, Mn, Fe, Cu, Zn, Al, Si, P and S were measured with inductively coupled plasma optical emission spectrometry (ICP-OES, iCap7400 Duo MFC, Thermo Fisher Scientific, Waltham MA, USA). Ions of fluoride, chloride, bromide, nitrate, phosphate, sulphate, lithium, sodium, ammonium, potassium, magnesium, and calcium were measured by liquid chromatography (930 Compact IC Flex, columns: Metrosep A Supp 5 – 150/4.0 and Metrosep C6 – 250/4.0, Metrohm, Herisau, Switzerland). Total inorganic carbon (TIC), total organic carbon (TOC) and total nitrogen (TN) were measured with a total-organic-carbon analyser, equipped with a total nitrogen unit (TOC-L CPH with TNM-L ROHS, Shimadzu, Kyoto, Japan). TIC was measured as $CO_2$ after oxidation with $H_3PO_4$, and TOC was determined after removal of TIC from the solution with HCl.

## Results

### Cathodoluminescence of silica minerals and carbonates

Silica minerals and carbonates from the three crystallisation stages were studied by cathodoluminescence (CL) microscopy. All minerals show a dominant red luminescence, which grades to brownish red. Chalcedony (stage I) displays colloform or concentric growth fabrics in bright reddish and dark CL colours (Fig. 4b). These features are not visible under polarised light. In amethyst and colourless quartz (stage II), CL microscopy reveals primary structures such as growth zoning, expressed by the alternation of different reddish to dark brown colours (Fig. 5b). The tension areas in deformed crystals show patchy red CL colours, highlighting the braided trends of healed microfractures in bright red (Fig. 5b). Early calcite (stage I) and late calcite (stage III) display stronger luminescence than silica minerals. Early calcite shows homogeneous bright orange-red CL colours, while late calcite shows red and dark brown CL colours, highlighting growth and intra-crystalline strain zones (Fig. 5f).

## Fluid inclusions

Fluid inclusions were identified in minerals of all mineralisation stages of the geode filling in the three mineralised lava flows. They are trapped in early calcite (stage I), amethyst and colourless quartz (stage II), and late calcite (stage III). Fluid-phase petrography was performed according to van den Kerkhof and Hein (2001). Following the criteria of Roedder (1984), two types of fluid inclusions were distinguished, primary and pseudosecondary. Primary fluid inclusions are trapped during crystal growth under non-stress conditions. On the other hand, pseudosecondary fluid inclusions are spatially associated with sigmoidal, healed, growth-stress-related micro-fractures within single crystals. Both inclusion types formed at different moments of single crystal growth, and thus, provide information about the composition of the mineral-supplying solution and the formation temperature of the confining crystal host.

### Fluid-phase petrography

Primary fluid inclusions in early calcite (stage I) are exclusively one-phase liquid and distributed along growth planes (Fig. 6a). The shapes are irregular with typical length between 10 and 15 µm, reaching up to 70 µm.

In amethyst and colourless quartz (stage II), primary fluid inclusions are exclusively one-phase liquid, hosted mainly along growth planes or in isolated clusters. Inclusion length varies from approximately 1 to 40 µm, mostly irregular in shape (Fig. 7a, b). Pseudosecondary fluid inclusions are spatially associated with deformed zones within individual crystals, in which they are trapped along healed, growth-related microfractures (Fig. 7c – f). They are mostly one-phase liquid and subordinately, bi-phase (liquid–vapour), with the first group typically exhibiting smaller dimensions (1 – 40 µm and 1 – 270 µm, respectively) (Fig. 7e – f). Individual inclusions are normally irregular, but rarely show negative crystal shape. Bi-phase pseudosecondary inclusions display variable liquid-to-vapour volume fractions.

Primary fluid inclusions in late calcite (stage III) contain one-phase liquid and are grouped in clusters. Individual inclusions show mainly irregular shape and length ranging from 1 to 20 µm (Fig. 6b). Pseudosecondary fluid inclusions are predominantly one-phase liquid and aligned along healed microfractures. In general, they show irregular shape and length ranging from 1 to 35 µm (Fig. 6c, d). Bi-phase (liquid – vapour) pseudosecondary inclusions have rarely been observed in the same trails hosting one-phase fluid inclusions, suggesting local modification of individual inclusions.

### Microthermometry

About 250 fluid inclusions representing all three mineralisation stages were analysed by microthermometry, most of them in amethyst and colourless quartz (stage II), and subordinately in calcite (stages I and III). Samples from different flows (2, 3 and 4) show very similar results and are presented together. Approximately 90% of the studied inclusions were one-phase liquid, and thus, were analysed by means

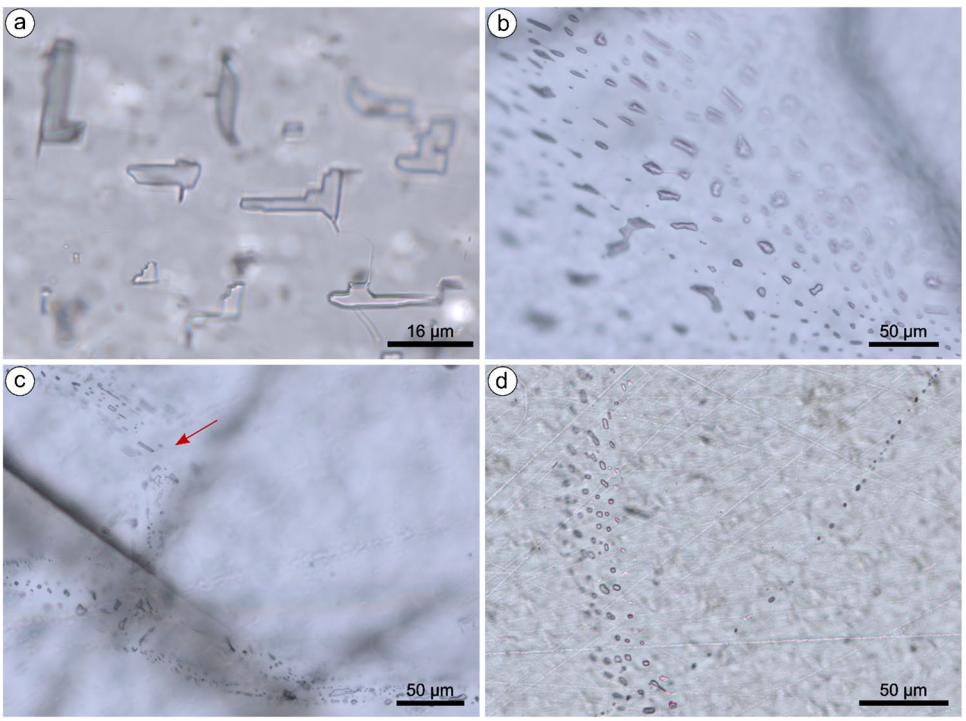


**Fig. 6** Photomicrographs of petrographic features of fluid inclusions (FI) in early (a) and late (b, c, d) calcite (stages I and III, respectively), plane-polarised light. **a** Primary one-phase FI in growth zone. **b** Cluster of primary one-phase FI. **c** Pseudosecondary one-phase FI hosted in healed fractures. **d** Details of pseudosecondary one-phase FI in healed fractures of single crystals

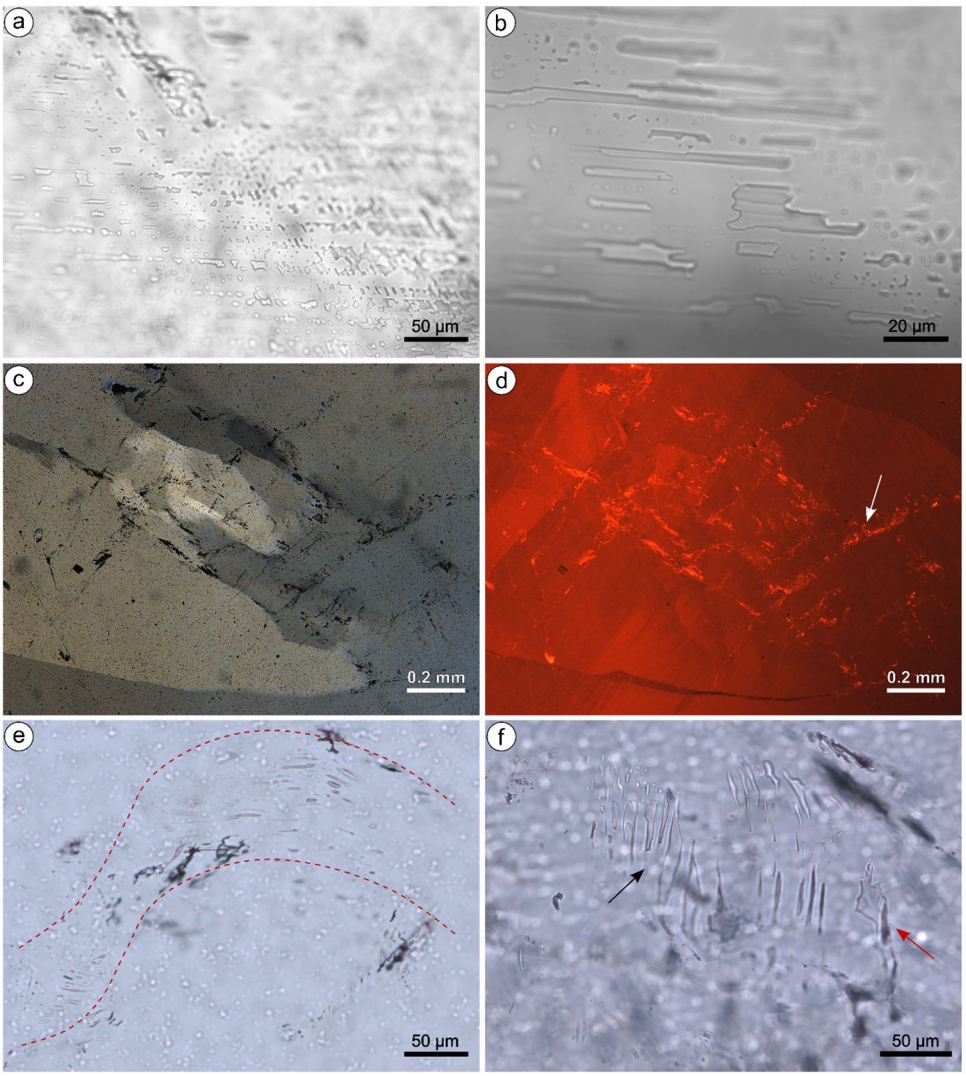


**Fig. 7** Photomicrographs of petrographic features of fluid-inclusion assemblages (FIA) in amethyst and colourless quartz (stage II) in relation to different microstructures, plane-polarised light and cathodoluminescence (CL). **a** Primary one-phase FIs in growth zone; **b** Detail of a. **c** Pseudosecondary one-phase FI spatially associated with healed microfractures in deformed zones of a single amethyst crystal, cross-polarised light. **d** Same field of view as shown in c under CL, highlighting deformation microstructures, such as healed microfractures (arrow). **e** Tension microstructures in single crystals hosting pseudosecondary FI. **f** Detail of one-phase (black arrow) and bi-phase (red arrow) pseudosecondary FI at room temperature, spatially associated to sigmoidal, growth-related microfractures

of nucleation-assisted microthermometry (Krüger et al. 2007). The remaining 10% of analysed inclusions were bi-phase (liquid–vapour). Total homogenisation temperatures and ice-melting temperatures (Tm-ice) were measured in all inclusions, while retrograde homogenisation temperatures ($Tht_r$) upon cooling were measured only in high-density inclusions with Tht < 55 °C. The occurrence of retrograde homogenisation is a consequence of the density maximum of water, and thus can, in addition to Tm-ice, be employed to assess the salinity of the aqueous solution based on the depression of the temperature of maximum density (TMD) (Marti et al. 2009). A summary of the microthermometry data of the initial one-phase fluid inclusions is displayed in Fig. 8. The complete data set is given in Supplementary Information (SI). The reported Tht values are corrected for the effect of surface tension on liquid – vapour homogenisation (Marti et al. 2012).

Total homogenisation temperatures of primary one-phase inclusions in early calcite (stage I) are between 30 and 87 °C, displaying a slightly skewed mode around 40 °C, and a second, minor mode around 80 °C (Figs. 8a, 9a). Average Tht of the low-temperature mode (excluding values > 70 °C) is 40.2 ± 7.0 °C (1SD). Values of Tm-ice measured in these inclusions are between -0.9 and 0 °C, and yield a mean value of -0.3 ± 0.2 °C (1SD) (Fig. 8e). Expressed in terms of wt% NaCl-eq., this corresponds to a mean salinity of 0.4 wt% NaCl-eq. and maximum salinities of up to 1.6 wt% NaCl-eq. (Fig. 9a).

Primary one-phase fluid inclusions in colourless quartz (stage II) display a broad range of Tht values, from 30 to 130 °C, with a weak frequency mode around 30 °C (Figs. 8b, 9a). The same wide scatter of Tht values was also observed in pseudosecondary one-phase inclusions, though with weak modes at higher temperatures, between approximately 85 and 120 °C (Fig. 8b, 9b). Variations of Tm-ice among different inclusions were found between -0.3 and -2.3 °C (Fig. 8f), corresponding to salinities from pure

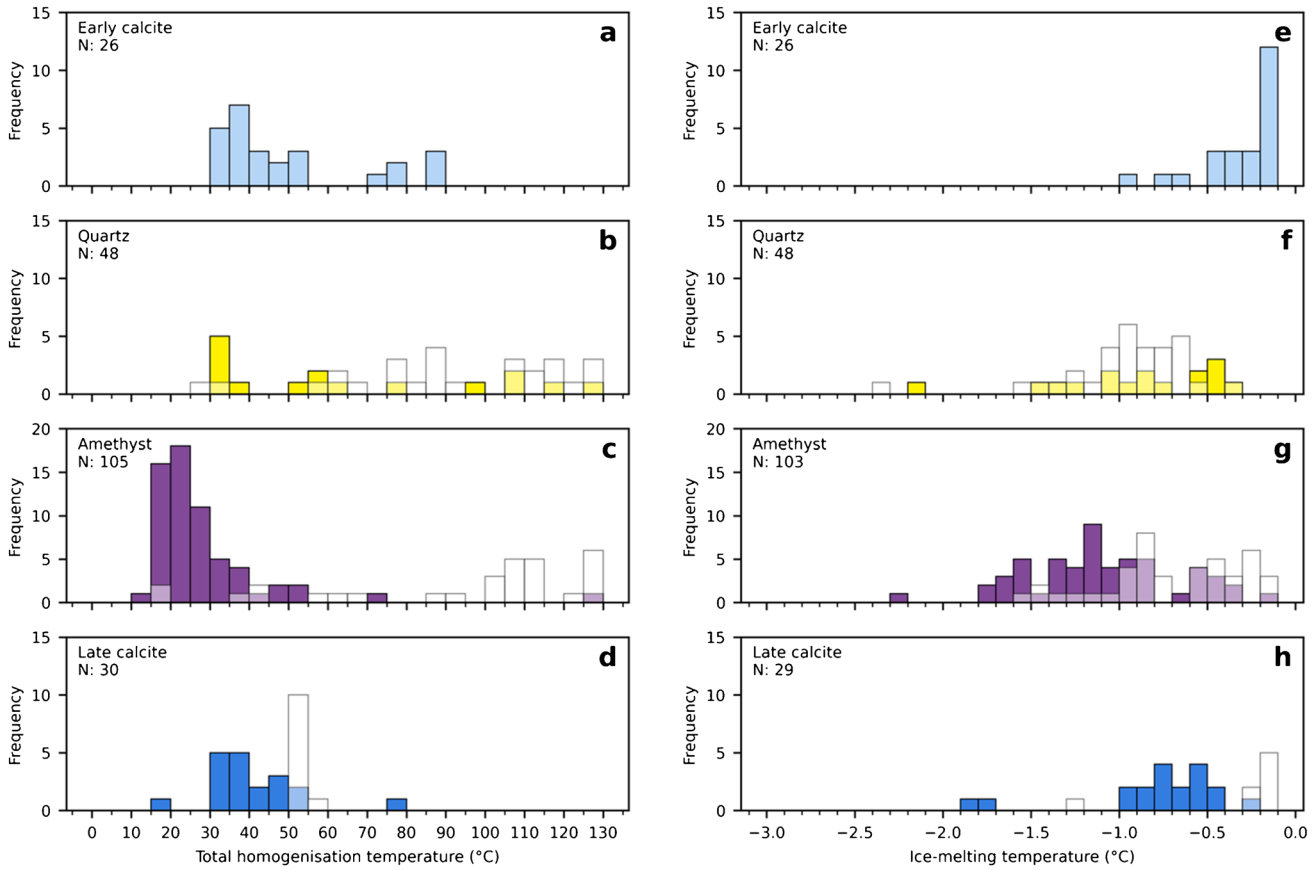


**Fig. 8** Distribution histograms of total homogenisation temperature (°C, left) and ice-melting temperature (°C, right) of initial one-phase fluid inclusions. Coloured bars: primary fluid inclusions; uncoloured bars: pseudosecondary fluid inclusions. **a, e** Early calcite – stage I. **b, f** Colourless quartz – stage II. **c, g** Amethyst – stage II. **d, h** Late calcite – stage III

water to maximum of 2.6 wt% NaCl-eq (Fig. 9). These data indicate a slight increase in the salinity of stage II.

Primary one-phase inclusions in amethyst (stage II) yield low Tht values between 15 and 55 °C, (Fig. 8c, 9a). Pseudosecondary one-phase inclusions, in contrast, show a wide range of Tht values between 16 and 130 °C, with predominantly temperatures of > 55ºC (Fig. 8c, 9b). In primary inclusions, Tm-ice mainly ranges from -0.1 to -1.7 °C while in pseudosecondary inclusions from -0.1 to -1.5 °C (Fig. 8g). This corresponds to salinities from pure water up to 3.0 wt% NaCl-eq. for primary and from pure water up to 2.6 wt% NaCl-eq. for pseudosecondary fluid inclusions in amethyst (Fig. 9).

Microthermometry was also attempted for pseudosecondary bi-phase fluid inclusions (L+V) of stage II, resulting in Tht values between 144 and 385 °C, which were not always reproducible. Observed Tm-ice values range from -1.3 to 0 °C, corresponding to salinities of up to 2.2 wt% NaCl-eq. However, the non-reproducible Tht data detected for most analysed pseudosecondary bi-phase fluid inclusions show evidence of partial leakage. The obtained temperatures are thus considered geologically meaningless, and are not further considered in the interpretation.

Total homogenisation temperatures of primary one-phase fluid inclusions from late calcite (stage III), show a clear mode between 30 and 55 °C (Fig. 8d, 9a). Excluding the outliers, the Tht range values is very similar to the Tht obtained for fluid inclusions in stage-I calcite. Pseudosecondary one-phase inclusions, in contrast, yield a small range with Tht values of 52.9 ± 1.0 °C (Figs. 8d, 9b). Values of Tm-ice for primary inclusions ranges from -0.2 to -1.8 °C, with a mode between -0.2 and -0.9 °C (Fig. 8h), discarding the two outliner, this corresponds to a salinity from pure water up to 1.5 wt% NaCl-eq. (Fig. 9a). Pseudosecondary inclusions, on the other hand, yield even higher Tm-ice, between -0.1 and -0.2 °C and, a single value of -1.2 °C (Fig. 8h). The salinity of the pseudosecondary inclusions in stage-III calcite corresponds from pure water up to 0.5 wt% NaCl-eq. (Fig. 9b). Generally, both generations of calcite (stages I and III) have similar Tht values and a slight difference in salinities, which are slightly lower than those displayed by amethyst and colourless quartz of stage II (Fig. 9).

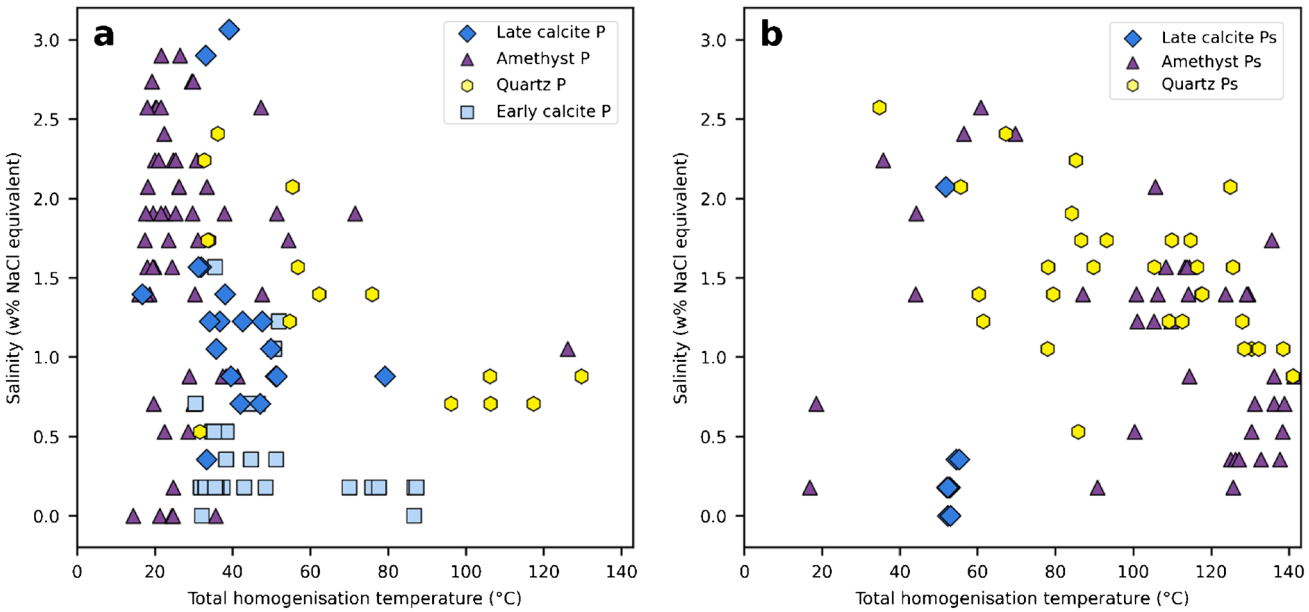


**Fig. 9** Plots of total homogenisation temperature (°C) vs. salinity (wt% NaCl-eq.) for all analysed **a** primary (P) and **b** pseudosecondary (Ps) fluid inclusions that are one-phase at room temperature

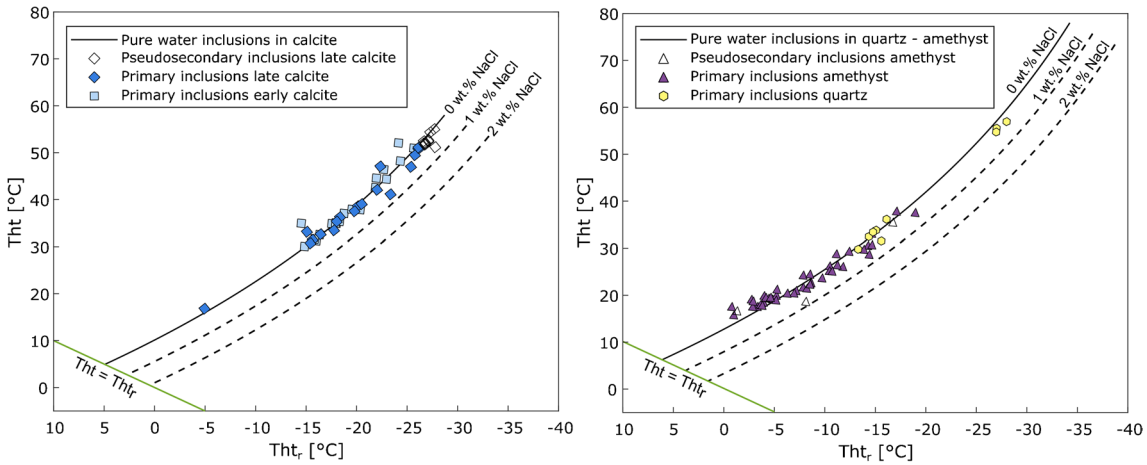


**Fig. 10** Plots of retrograde ($Tht_r$, °C) vs. prograde (Tht, °C) homogenisation temperatures for all analysed high-density fluid inclusions, initially one-phase aqueous, hosted in calcite (left) and, amethyst and quartz (right). The intercepts for the temperatures of maximum density (TMD) of water for calcite and quartz, where $Tht_r = Tht$, correspond to values between 5.1 and 4.9 °C, and 6.15 °C, respectively, according to Marti et al. (2009). For comparison, we have plotted the corresponding Tht – $Tht_r$ curves for 1 and 2 wt.% NaCl eq. solutions

The relation between prograde (Tht) and retrograde homogenisation temperature ($Tht_r$) is controlled by the temperature of maximum density (TMD) of the aqueous solution and by the thermal volume expansion of the confining host mineral. Since the TMD decreases as a function of salt concentration and composition, Tht – $Tht_r$ pairs provide a second measure of the salinity of high-density one-phase fluid inclusions (Marti et al. 2009; Gilg et al. 2014), in which retrograde homogenisation occurs before ice nucleation (Tn-ice) ($Tht_r > Tn\text{-ice}$).

Measured Tht – $Tht_r$ pairs of primary and pseudosecondary inclusions are shown in Fig. 10 separated between calcite- and quartz-amethyst-hosted inclusions. The black curves represent the calculated Tht – $Tht_r$ relation for calcite- and quartz-confined pure water systems using the IAPWS-95 formulation (Wagner and Pruß, 2002), and thermal expansions coefficients of the respective host mineral. The green line indicates equality of Tht and $Tht_r$ ($Tht = Tht_r$). In the calcite-confined pure water system, the Tht – $Tht_r$ curve ends at 4.9 °C, the temperature at which Tht and $Tht_r$ become

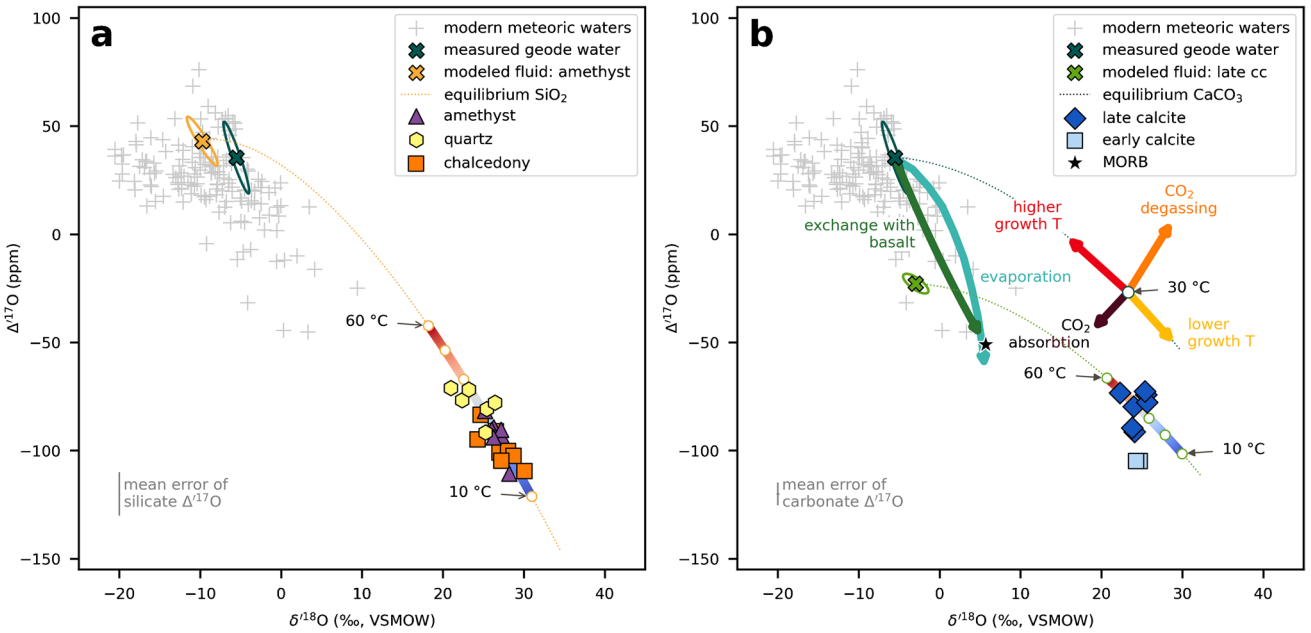


**Fig. 11** Plots of $\delta^{18}O$ vs. $\Delta'^{17}O$. **a** Silica minerals. **b** Carbonates. The global dataset of meteoric water was extracted from Luz and Barkan 2010 and Aron et al. 2021. Dashed lines: equilibrium line for quartz – water and calcite – water. Schematic vectors in b indicate shifts in isotopic signatures due to different geological processes that can move the carbonates away from equilibrium

equal. In the quartz-confined system, in contrast, this temperature plots at 6.15 °C, and in a true isochoric system ends at 3.98 °C. The diagrams reveal that most of the data points plot close to the pure water curve, indicating very low salinity. We note, however, that a relatively large portion of the Tht – $Tht_r$ data, both from calcite- and quartz-hosted inclusions, plot on the left-hand side of the pure water curve, indicating seemingly negative salinities. This inconsistency likely results from random deviations of the actual volume change of the inclusions from the calculated thermal expansion of the host mineral. Pairs plotting on the left-hand side of the pure water curve were previously reported from synthetic fluid inclusions quartz (Qiu et al. 2016), and from fluid inclusions in stalagmites (Pasqualetto et al. 2023). For calculations of the fluid salinities, we had to discard this data points.

Using experimental data of the TMD of aqueous solutions as a function of NaCl concentration compiled from the literature, we compared the salinity of the inclusions with those derived from Tm-ice measurements. Significant differences in salt concentration obtained with the two methods are observed (Fig. 1 SI), with higher and more variable values derived from Tm-ice and lower, more consistent values derived from Tht – $Tht_r$ measurements. The difference between the two data sets was also observed by Gilg et al. (2014).

In summary, the mineralising fluids can be described as very low saline aqueous solutions and no significant salinity changes occurred from stage I to stage III of the mineralisation sequence. Assuming that the fluid was undersaturated with respect to dissolved gases at the p – T conditions of mineral formation, the thermodynamic properties of the fluid can be approximated by a gas-free $H_2O$ – NaCl system.

## Stable isotopes

Measurements of oxygen isotopes were carried out in carbonates and silica minerals including chalcedony, coarse-grained colourless quartz and amethyst. The samples comprise the three crystallisation stages of the typical geode mineralisation sequence (Fig. 3). In addition, water samples collected from groundwater boreholes and geodes were also analysed. All carbonate samples were also analysed for carbon isotope compositions. The results are given in Supplementary Information, with $\delta^{18}O$ and $\Delta'^{17}O$ reported relative to VSMOW, $\delta^{13}C$ normalized to the VPDB, and deuterium expressed in ‰. Isotopic signature trends are observed within the different crystallisation stages in the geodes, but no significant variations are recorded between samples from different lava flows.

### Triple oxygen isotopes

**Water samples** Triple-oxygen-isotope values for water samples yield a small range with only slight differences between different samples (Fig. 11). Geode-hosted water samples

yield $\delta^{18}O$ values from -5.0(±0.1)‰ to -4.6(±0.1)‰, and $\Delta'^{17}O$ values of 0.03(±0.01)‰, while the present-day groundwaters hosted in fractured basaltic aquifer show slightly more negative $\delta^{18}O$ values between -6.5(±0.5)‰ and -5.5(±0.1)‰, and $\Delta'^{17}O$ of 0.04(±0.1)‰ (Table 2 SI). In Fig. 11, these values are contrasted with global meteoric water data from Luz and Barkan (2010) and Aron et al. (2021).

**Silica minerals** The $\delta^{18}O$ oxygen isotopic compositions of all minerals range from 21.2(±0.2)‰ to 30.5(±0.2)‰, and $\Delta'^{17}O$ values vary between -0.10(±0.01)‰ and -0.07(±0.01)‰ (Table 3 SI). Chalcedony (stage I) displays the largest variation in $\delta^{18}O$, between 24.6(±0.2)‰ and 30.6(±0.2)‰. Except for sample UYFAR-1A, subsequent fine-grained colourless quartz (stage II) exhibits lower $\delta^{18}O$ values than chalcedony within the same sample, with values ranging from 21.2(±0.2)‰ to 26.8(±0.2)‰. In contrast, subsequent amethyst crystals (stage II) display a light enrichment in $\delta^{18}O$ composition relative to colourless quartz from the same sample, with smaller variations between 26.7(±0.2)‰ and 28.6(±0.2)‰. Zoned colourless quartz-amethyst crystals yield $\delta^{18}O$ values of 26.7(±0.2)‰ and 26.8(±0.2)‰ respectively, showing a constant isotopic composition throughout the crystals. In general, a trend is observed where chalcedony and amethyst have higher $\delta^{18}O$ and lower $\Delta'^{17}O$ in respect to colourless quartz (Fig. 11a).

**Carbonates** Early calcite (stage I) shows $\delta^{18}O$ values between 24.7(±0.3)‰ and 25.1(±0.1)‰, and $\Delta'^{17}O$ values of -0.10(±0.01)‰. Late calcite (stage III) yields $\delta^{18}O$ values similar to the early calcite, ranging from 24.1(±0.3)‰ to 26.1(±0.1)‰, and higher $\Delta'^{17}O$ values from -0.09(±0.01)‰ to -0.07(±0.01)‰ (Fig. 11b, results are given in Table 4 SI). In general, all calcite $\delta^{18}O$ values are slightly lower than those for silica minerals.

**Equilibrium models** In order to estimate the composition of the fluids from which the minerals crystallised, water – mineral equilibrium models were calculated for the dataset (Fig. 11). The $\delta^{18}O$ value of a mineral is a function of the starting $\delta^{18}O$ composition of the fluid from which the mineral crystallised and of the temperature-dependent fractionation factor between quartz and water, or between carbonate and water. To estimate the crystallisation temperature of different silica phases, the quartz – water equilibrium equation of Sharp et al. (2016) was used. For carbonates, we used the oxygen-isotope-fractionation equations for calcite – water systems of Daëron et al. (2019) and Wostbrock et al. (2020b).

To estimate the oxygen isotope composition of the original fluids, best-fit equilibrium models were calculated for which the calculated temperatures best agree with the corresponding crystallisation temperatures estimated from fluid inclusions (see Supplementary Information). Conspicuously, the water samples from geodes and groundwater are very similar to the modelled fluid for the silica minerals. The excellent agreement of triple-oxygen-isotopes data of all silica minerals over the quartz – water equilibrium curve supports the crystallisation from fluids with a unique composition at temperatures fluctuating between approximately 15 and 40 °C during the different crystallisation stages. In detail, estimated crystallisation temperatures of chalcedony and early calcite from stage I are between 15 and 35 °C, and approximately 20 °C, respectively. In stage II, the temperatures range from 25 to 40 °C for colourless quartz and from 15 to 35 °C for amethyst. For late calcite (stage III), estimated crystallisation temperatures range from 25 to 60 °C. On the other hand, the isotope signatures from calcite are not as well aligned as the silica minerals and do not overlap with the present-day geode water (see discussion).

## Carbon isotopes

Carbon isotopic compositions show slight differences between early (stage I) and late (stage III) calcite. $\delta^{13}C$ values of early calcite display a small range between -9.39(±0.01)‰ and -9.21(±0.01)‰, while late

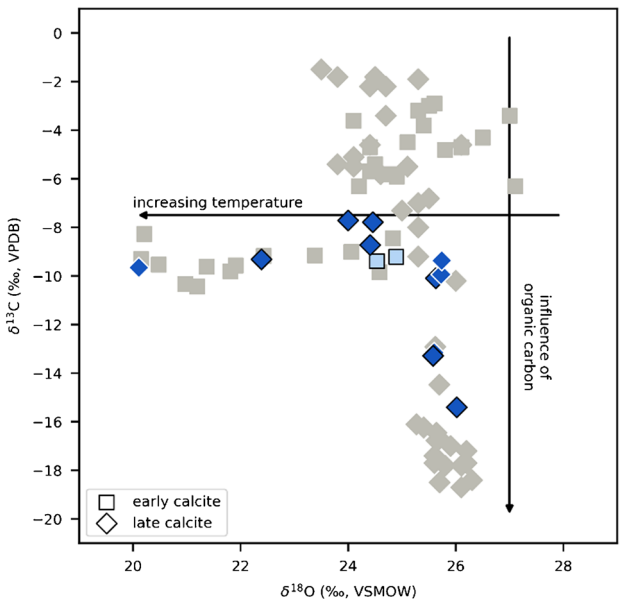


**Fig. 12** Plot of $\delta^{18}O$ vs. $\delta^{13}C$ in carbonates. Coloured symbols: present study; grey symbols: data from literature (Gilg et al. 2003; Morteani et al. 2010). Variations in $\delta^{18}O$ and $\delta^{13}C$ values respectively indicate changes in temperature and influence of the carbon source

calcite presents a larger range, from -15.41(±0.01)‰ to -7.79(±0.01)‰ (Fig. 12, results in Table 5 SI).

#### Deuterium

Measurements of deuterium were carried out in the same water samples that were used for triple oxygen isotopes, including samples of geode-hosted and groundwater from the basaltic aquifer. Geode-hosted yields $\delta^2H$ values of -30.8(±0.6)‰ and $\delta^{18}O$ of -4.3(±0.1)‰, while groundwater yield $\delta^2H$ values between -30.0(±1.4)‰ and -27.9(±1.2)‰, and $\delta^{18}O$ values from -5.5(±0.1)‰ to -4.9(±0.2)‰ (Table 6 SI). Regardless of the kind of sample, the results are in the field of the global meteoric water dataset (Craig 1961).

### Hydrogeochemistry and silica geothermometers

The same water samples analysed for triple oxygen isotopes and deuterium were also analysed for major ions and trace-element concentrations in addition to pH measurements (Table 7, 8 SI). The groundwater samples from the study area present calcic to sodic-bicarbonate affinity. Major-ion concentrations are in the range of: 8 – 45 mg $L^{-1}$ Na; 0.5 – 1.4 mg $L^{-1}$ K; 6.4 –13.2 mg $L^{-1}$ Mg; 22.3 – 40.3 mg $L^{-1}$ Ca; 0.5 – 6.4 mg $L^{-1}$ Cl; 0.4 – 26.7 mg $L^{-1}$ $SO_4$; 24.5 – 54.2 mg $L^{-1}$ $HCO_3 + CO_3$; 0.3 – 3.9 mg $L^{-1}$ $NO_3$; 19.2 – 24.2 mg $L^{-1}$ Si and 0.1 – 0.6 mg $L^{-1}$ F. Geode-hosted water (UYFAR-11–2) presents somewhat similar chemical composition to the groundwater samples, though differing in their slightly to moderately higher concentrations of $SO_4$, Cl, F, Na and S, and a depletion in Si, Ca and K. Sample UYFAR-10 was already opened at the sampling time, therefore, the high contents of $NO_3$ could respond to contamination with explosives used for the extraction (ANFO: Ammonium Nitrate $NH_4NO_3$—Fuel Oil; TNT or gunpowder which contains $KNO_3$). Consequently, this sample was not considering in the data interpretation. Values of pH are from 7.2 to 8.0 in groundwater samples, while geode-hosted water has a pH of 7.5.

Concentration of silica in water is a function of $SiO_2$ solubility, which is strongly temperature-dependent (e.g., Williams et al. 1985). Application of silica geothermometers (Fournier 1977) to silicon concentrations in groundwater samples between 19.2 and 23.2 mg $L^{-1}$ yield precipitation temperatures between 30 and 39 °C for amorphous silica and between 62 and 70 °C for quartz. These temperatures correspond to the best direct estimation for the precipitation of silica during the earliest stage. Amorphous silica is assumed to be the precursor phase at an early stage of the mineralisation. The geode-hosted water which has silica concentrations below to the limiting factor of $SiO_2$ precipitation (< 7 mg $L^{-1}$ Si) is not contemplated for these calculations.

## Discussion

Fluid-inclusion and stable-isotope data from the amethyst and agate geodes show slight differences between different crystallisation phases of the geode filling, as exemplified in Figs. 8, 9, 11 and 12. However, there is a conspicuous lack of systematic variations between the different mineralised lava flows, which suggests that the mineralisation is neither controlled by magmatic processes, nor by the composition of the basaltic host of the geodes. Rather, because the mineralisation is similar in all the mineralised flows and the characteristics of the mineralising fluids are essentially identical, we conclude that the geode fillings formed after the emplacement of the entire basaltic sequence in pre-existing volcanic cavities. These cavities are widely accepted as a product of gas exsolution, in a supersaturated magma during cooling, with coalescence and accumulation of the ascending gas in the upper part of the flow (e.g., Leinz 1949; Sparks 1978; Corrêa et al. 1994; Gomes 1996; Scopel et al. 1998; Juchem 1999; Proust and Fontaine 2007a; Götze et al. 2016). A host-independent crystallisation for Los Catalanes was proposed also by Duarte et al. (2011), based on $\delta^{18}O$ compositions of silica minerals and carbonates from flows 3 (Catalan) and 4 (Cordillera). This interpretation also applies to the scale of the Paraná-Etendeka LIP, since the two most important amethyst deposits in Uruguay and Brazil are hosted by basaltic lavas in different stratigraphic positions and with contrasting first-order chemical signatures within the PLIP (Bellieni et al. 1984; Peate et al. 1992). While the deposits in Uruguay are hosted by low-Ti lavas (< 2 wt.% $TiO_2$, Hartmann et al. 2010), the ones in Brazil occur in high-Ti lavas (2–4 wt.% $TiO_2$, Gilg et al. 2003; Hartmann et al. 2010, 2014).

The main topics discussed below are the temperatures during mineralisation and the origin and composition of the mineralising fluid, profiting from the application of state-of-the-art analytical methods including nucleation-assisted microthermometry of one-phase fluid inclusion and triple oxygen isotope geochemistry.

### Mineralisation temperatures

The predominance of one-phase liquid fluid inclusions at room temperature suggests low-temperature crystallisation conditions close to the surface (Roedder 1984). Based on the observation of one-phase inclusions in amethyst from Uruguay and Brazil, other studies also suggested low crystallisation temperatures (Juchem 1999; Gilg et al. 2003; Commin-Fischer et al. 2010; Morteani et al. 2010; Duarte et al. 2011), though without specific constraints. Microthermometry of

such metastable fluid inclusions is limited by the lack of a stable vapour phase using traditional analytical techniques. Precise microthermometry of one-phase liquid inclusions, achieved by the nucleation of a vapour bubble with a femtosecond laser pulse (Krüger et al. 2007) was previously accomplished by Gilg et al. (2014) for the Brazilian deposits. The latter authors proposed mineralisation temperatures fluctuating between 40 to 90 °C.

Total homogenisation temperatures (Tht) of primary fluid inclusions provide an estimate of the minimum formation temperature of the host mineral, given that the fluid inclusion volumes have not been modified during post-formation processes (Roedder 1984). The density of the enclosed fluid, and hence Tht, depends on formation temperature and pressure of the inclusion, which therefore requires estimating one of the two variables to calculate the other based on the slope of the fluid isochore. Variations of Tht can therefore indicate both changes of the fluid temperature and/or of the fluid pressure. However, giving the lack of stratigraphic constrain, no pressure correction was applied. The crystallisation temperatures estimated from the primary fluid inclusions suggest mineralisation temperatures mostly in the range of 15 – 60 °C (Figs. 8, 9). Temperatures for the different crystallisation stages range from 25 to 55 °C for stage I (early calcite), 30 to 60 °C and 15 to 55 °C for stage II (quartz and amethyst respectively), and 17 to 55 °C for stage III (late calcite). Fluctuations in the hydrostatic pressure would result in slightly higher fluid-trapping temperatures. Outlying homogenisation temperatures higher than 60 °C (Fig. 9) in primary fluid inclusions may be the result of stress during crystal growth – e.g., due to crystals competing for limited space in the transition from fine- to coarse-grained quartz. On the other hand, the low crystallisation temperatures estimated agree with the lack of evidence of re-equilibration of fluid inclusions, which would result in significantly higher Tht values, particularly in the more reactive calcite. This discard possible post-crystallisation heating, which agrees with the assumption that the mineralisation took place after the final emplacement of the basaltic sequence. The skewed distribution of Tht can thus be interpreted as a record of an ascending warm fluid that equilibrated with the surrounding wall rock.

The low temperatures are consistent with the present-day geothermal gradient of the Guarani aquifer hosted in sediments below approximately 1,700 m of basaltic pile, as determined from the temperature of water produced by geothermal wells along the Uruguay/Argentina border, which is of 32 °C/km (Morteani et al. 2010). In addition, recent studies have demonstrated the potential for intermediate-temperature geothermal systems spatially associated with the deepest structural levels of the north-western region of the Paraná Basin in Uruguay, with estimated temperatures of about 95 °C at depths close to 3.500 m (Morales et al. 2021). Our low-temperature estimates are in strong contrast with the higher temperatures (200 – 300 °C) suggested by Proust and Fontaine (2007b), who proposed an exclusively magmatic origin for the mineralisation. Such outlying high temperatures may result from the microthermometry of leaked bi-phase fluid inclusions, which do not represent the crystallisation temperatures. Data obtained from bi-phase fluid inclusions in the present study achieved homogenisation temperatures that are similar to the values reported by those authors. However, because most of these inclusions show evidence of leakage and did not yield reproducible values, we do not consider them as representative estimates for the crystallisation conditions of the geodes.

On the other hand, pseudosecondary one-phase fluid inclusions typically display a larger range and overall higher total homogenisation temperatures compared to the primary fluid inclusions (Fig. 9), with temperatures between 15–130 °C. This systematic difference indicates a modification of the fluid inclusions after their initial entrapment due to intracrystalline deformation (Roedder 1984). These fluid inclusions are related to deformed areas of individual crystals, in which the inclusions are trapped within healed, growth-related microfractures (Fig. 7c, d, e). The systematic shift from lower temperatures in the primary one-phase liquid fluid inclusions to higher temperatures in pseudosecondary one-phase liquid fluid inclusions, and even higher in pseudosecondary bi-phase fluid inclusions, suggests a continuous trend of modification of the primary inclusions through stretching and leakage due to intracrystalline deformation during growth (Fig. 9).

In contrast to Tht values, triple-oxygen-isotope data are independent of pressure, and therefore provide real mineral formation temperatures. The crystallisation temperatures calculated by the equilibrium models based on our data are in excellent agreement with the primary fluid-inclusion temperatures. We found that the silica minerals formed from fluids with similar isotopic composition to groundwater and geode-hosted water. Equilibrium modelling of the triple-oxygen-isotope data performed by calibrating the equilibrium curve of Sharp et al. (2016), along with data corresponding to a temperature range of 15 – 40 °C, results in a starting fluid signature that is very similar to the measured groundwater (Fig. 11). Using this water composition, the triple-oxygen-isotope data allows to estimate the crystallizing temperature of chalcedony from stage I (15 – 35 °C), which was not possible to acquire using fluid-inclusion microthermometry, as the microcrystalline structure of the mineral prevents the entrapment of fluid inclusions (e.g., Götze et al. 2020). These results are slightly colder than the temperatures suggested by the crystallisation temperature of the accessor mineral paragenesis observed in direct contact with the basalt in stage I (celadonite, 22 to 60 °C Duplay et al. 1989, zeolite-heulandite, > 50 °C Apps 1983, smectite,

**Table 2** Summary of forming temperatures estimated with the different applied methods

| Minerals | Estimated forming temperatures (°C) | | |
|---|---|---|---|
| | Nucleation-assisted microthermometry | Triple Oxygen Isotopes | Silica geothermometers of groundwater |
| Amorphous silica | | | 30 – 39 |
| Chalcedony/Agate | | 15 – 35 | |
| Early calcite | 25 – 55 | 20 – 30 | |
| Colourless quartz | 30 – 60 | 25 – 40 | 62 – 70 |
| Amethyst | 15 – 55 | 15 – 35 | |
| Late calcite | 17 – 55 | 25 – 60 | |

25 to 170 °C Chipera and Apps 2001). This may suggest a participation of low temperature hydrothermal alteration at the earliest stage of the mineralisation followed by cooling. The crystallisation of quartz at stage II indicates higher temperatures than chalcedony at stage I (Fig. 11). All the silica minerals plot in a trend aligned with the quartz – water equilibrium curve (Fig. 11a), suggesting that chalcedony, colourless quartz, and amethyst crystallised from one evolving fluid. Calculated temperatures using silica geothermometers (Fournier 1977) also yield crystallisation temperatures between 30 and 39 °C for amorphous silica, and between 62 and 70 °C for quartz. These temperatures support the low temperatures estimated by microthermometry and triple oxygen isotopes (Table 2).

## Source of the mineralising fluid

Our data provide valuable information about the possible origin of the mineralising fluid. Compositions recorded for the fluid inclusions are in the range of meteoric water, with salinities close to pure water. Salinities calculated with the Tht – $Tht_r$ method (TMD) yield rather constant values below 1 wt% NaCl-eq. (Fig. 10). This is consistent with present-day groundwater. On the other hand, ice-melting temperatures indicate slightly higher salinities (up to 3 wt% NaCl-eq.), which show a systematic variation with the lowest salinities for calcite from stages I and III (up to 1.6 wt% NaCl-eq.). These values are in accordance with the low salinities reported in previous studies of Brazilian amethyst deposits (Commin-Fischer et al. 2010). Gilg et al. (2014) reported slightly higher salinities (up to 5.3 wt% NaCl-eq.) in Brazil, decreasing from early to late mineraliszation stages, interpreted as different fluid generations. Neither such high salinities nor such systematic trends have been observed in the samples from Uruguay.

In accordance with the fluid-inclusions data, triple-oxygen-isotope signatures show excellent agreement between the modelled crystallisation fluid and meteoric water. Silica minerals plot remarkably well in a trend along the quartz – water equilibrium curve, suggesting a sequence of crystallisation from the same original fluid. Triple-oxygen-isotopic signatures of water samples are within the range of a global dataset for meteoric water (Fig. 11; Luz and Barkan 2010; Aron et al. 2021), and do not show substantial differences between the geode-hosted water and the present-day groundwater from the basaltic aquifer. Moreover, hydrogeochemistry and deuterium data from geode-hosted water and groundwater from this study also show affinity with meteoric water, suggesting that they may have a similar composition as the water from which the silica minerals formed, in spite of the low groundwater percolation rates in basalt. The deuterium–oxygen results from groundwater, allows to establish a meteoric water baseline for the time of the sample collection, which is not aligned with the results from the geode-hosted water collected during the same campaign (Fig. 7 SI). The small shift from this meteoric baseline between the groundwater and the geode-hosted water suggests that the interconnectivity between groundwater and the geode water is not instantaneous and that some time is needed for the water to percolate from the groundwater to the geode. Our geode water $\delta^{18}O$ and $\delta^{2}H$ data shows good agreement with data reported from geodes from Brazilian deposits (Matsui et al. 1974).

On the other hand, $\delta^{13}C$ values in carbonates are heterogeneous, suggesting variable sources for the carbon in the fluids. The low $\delta^{13}C$ values, from -7.8 to -15.5‰ (Fig. 12), indicate that organic matter may have affected the isotopic composition of the mineralising fluid. Organic matter could be transported in solution from the different underlying units of the Paraná Basin, which represents an ample source of organic matter (e.g., Veroslavsky et al. 2021), or from the overlying soil. On the other hand, Gilg et al. (2003) and Morteani et al. (2010) reported higher values of $\delta^{13}C$ for the Brazilian and Uruguayan deposits respectively, suggesting a contribution of magmatic carbon from the basalts (Fig. 12).

It is important to note that the mineralising fluid was saturated in silica in order to crystallise the remarkable association of silica minerals. As suggested in previous studies (e.g., Gilg et al. 2003), possible sources for the silica could be altered glass in the mesostasis of the host basalts, or the underlying and inter-trap sandstones of the Mesozoic Tacuarembó and Rivera formations. Silica concentration of 23 mg $L^{-1}$ in borehole water samples from the basaltic aquifer analysed in the present study agrees with the concentrations reported for the upper Guaraní aquifer hosted in sandstones underlying the basalts (20 – 22 mg $L^{-1}$), which is saturated in silica relative to quartz (Arújo et al. 1999; Morteani et al. 2010). Our hydrogeochemical analysis of geode-hosted water shows similar composition as the groundwater samples, though with a $SiO_2$ depletion (7 mg

$L^{-1}$) suggesting that the water had already experienced $SiO_2$ crystallisation. The groundwater and geode-hosted water analyses, as well as fluid-inclusion and stable isotope compositions, indicate that the mineralising fluid was similar to present-day groundwater.

## Calcite crystallisation

In contrast to the silica minerals, the triple-oxygen-isotope data from the geode carbonate do not align with the calcite – water equilibrium curve (Fig. 11b). Two possible causes that may lead to a shift of the data from the equilibrium curve are: (1) crystallisation of the calcite under out-of-equilibrium conditions from a fluid with an isotopic signature compatible with that of the silica minerals, or (2) crystallisation in equilibrium from fluids with different oxygen isotopic signatures than those of the fluid from which the silica minerals crystallised.

In the first case, if the carbonate crystallised out of equilibrium from a starting fluid with a similar isotopic composition to that of the silica minerals, the shift in the isotopic signatures must be attributed to kinetic processes during the course of crystallisation inside the geodes, moving the data from the carbonate away from the equilibrium curve. Kinetic fractionation during carbonate formation – i.e., due to $CO_2$ degassing or absorption – could cause shifts in the oxygen isotope signatures. In the case of $CO_2$ degassing, this would result in higher $\delta^{18}O$ and higher $\Delta'^{17}O$, thus shifting the samples in a direction opposite to the shift observed between the carbonate and silica minerals in Fig. 11. In the case of $CO_2$ absorption, kinetic effects would shift the carbonate values to lighter $\Delta'^{17}O$ and $\delta^{18}O$ (Guo and Zhou 2019; Herwartz 2021; Bajnai et al. 2024), as illustrated in Fig. 11b. However, $CO_2$ absorption requires high pH fluids, implying that the shift depends on the pH of the solution and the speed of precipitation. In the case of the geode mineralisation, this would require very fast precipitations at very high pH (Guo and Zhou 2019; Herwartz 2021; Bajnai et al. 2024) – i.e. crystallisation involving two different fluids with contrasting pH, as well as contrasting precipitation rates, and/or temperature conditions. In addition, carbonates precipitating in basalt upon the injection of $CO_2$-rich water forms close to isotope equilibrium (Holdsworth et al. 2024). Therefore, none of these scenarios can satisfy the carbonate precipitation.

In the second case, if the carbonate crystallised from fluids with different oxygen isotopic signature from the silicate-forming fluids, this would result in a considerable shift of the original isotopic signature of the carbonates ($\delta^{18}O$ of $-5 \pm 2‰$ and $\Delta'^{17}O$ of $-50 \pm 5$ mg $L^{-1}$) relative to present-day groundwater. Higher evaporation rates may explain the shift in surface and groundwater (Aron et al. 2021) – e.g., by changing the regional climatic conditions, leading to different isotopic composition of the recharging fluids in the aquifers. This would imply that the crystallisation of silica minerals and calcite was associated with different climatic conditions, and would thus require a time gap. In addition, this would mean that each crystallisation stage was restricted to specific periods in time. Alternatively, the fluids may originate from different aquifers without mixing.

Another possible process is water – rock interaction. The expected geochemical effect of such an interaction is a shift of the oxygen isotope ratios of the host rock and/or the water away from their initial values (Fig. 11b). Variable fluid flux from the deepest part of the Paraná Basin over time may cause different rates of water – rock interaction and therewith changes of the isotopic composition within the aquifer. This has been observed in modern geothermal systems of Iceland, which yield similar results though at higher temperatures (250 – 400 °C, Zakharov et al. 2019; Wostbrock et al. 2018). In addition, water – rock interaction would increase the alkalinity of the fluid, which is a prerequisite for carbonate formation. In this case, we expect precipitation of silica minerals being controlled by a rapid fluid flux with very low water – rock interaction, resulting in a fluid with isotopic composition similar to that of present-day groundwater. On the other hand, carbonates may have precipitated from fluids that experienced lower fluid flux and thus a prolonged water–rock interaction. Fast and slow water fluxes could have alternated leading to carbonate and silica mineralisation during the same stage of crystallisation, which is consistent with our observations. Scatter in the calcite $\Delta'^{17}O$ values could thus be a result of different extent of water–rock interaction.

## Implications for the mineralisation process

The present fluid-inclusion and isotope data indicate that the crystallisation of the minerals inside pre-existing cavities is the result of a continuous process. In this scenario, the infiltration rate of mineralising fluid into the geodes is controlled by the low permeability of the host rock, dependent on the connection between vesicles, microfractures and the reactivation of previously sealed faults and fractures within the basalt. The intermittent fluid supply into the geodes resulted in a heterogeneous deposit, in which some geodes have multiple crystallisation stages and others have only one, or can even be empty. Low temperatures (< 60 °C), salinities from pure water up to 3 wt% NaCl-eq., and silica enrichment of 23 mg $L^{-1}$ $SiO_2$ estimated for the mineralising fluid can be achieved by remobilization of groundwater at medium to deep levels of the Parana Basin (max. of 3500 m in Uruguay, Fig. 13a). The reactivation of first-order regional structures is not only responsible for the deposition of the volcano-sedimentary sequence (e.g., Rostirola et al. 2000; Holz et al. 2006; Strugale et al. 2007; Hueck et al. 2017,

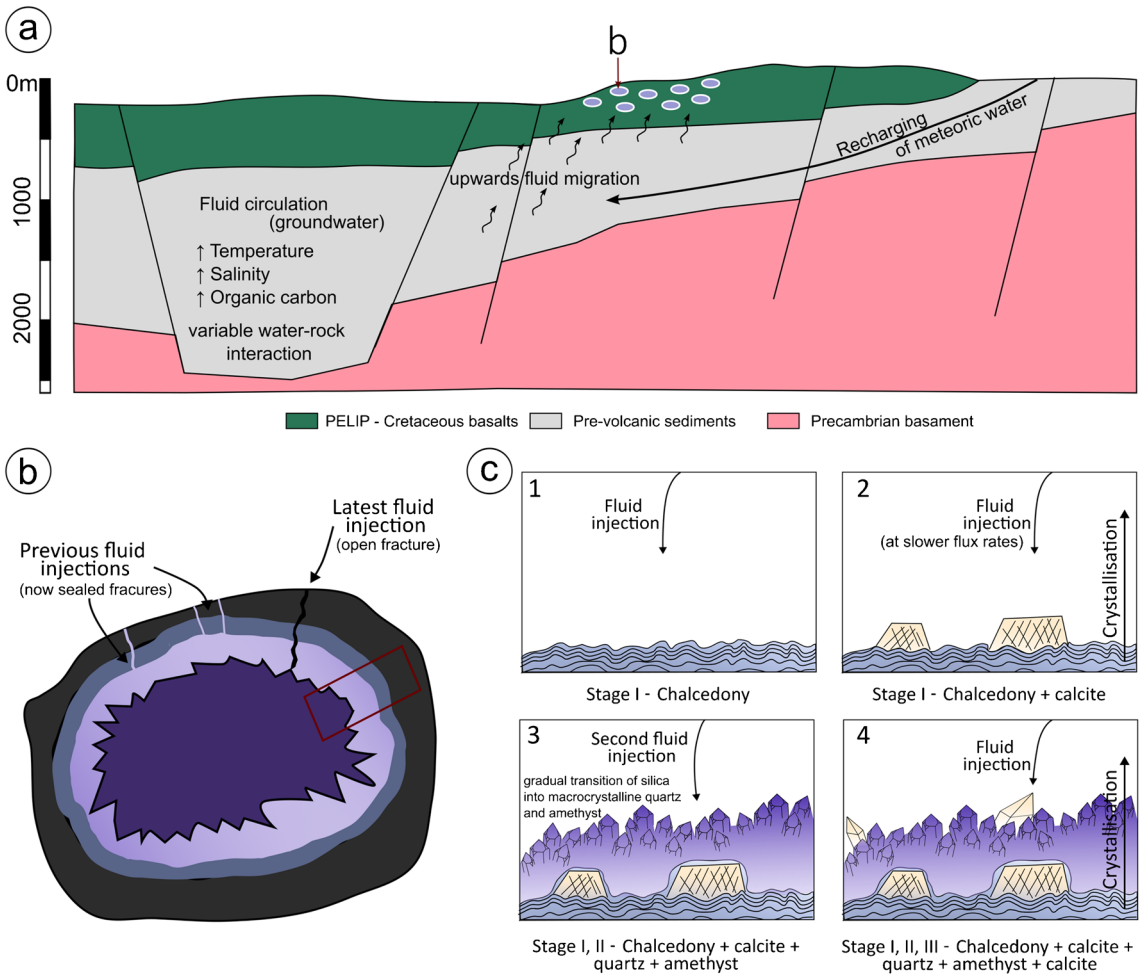


**Fig. 13** Proposed mineralisation model. **a** Groundwater circulation from the deepest part of the Paraná Basin, ascending to the host rock by fault reactivation; **b** Mineralising fluid reaching pre-existing cavities in an episodic alternation between open and closed system; **c** detail of b, crystallisation of mineral phases

2020; Veroslavsky et al. 2021; Morales et al. 2021), but may also control groundwater remobilization. Macro- and microfractures, possibly caused by the reactivation of the regional structures, may be responsible for providing the pathways for replenishing and interconnecting the pre-existing vesicles (Fig. 13a, b). In some cases, the vesicles have not been mineralised, indicating that they were completely isolated. Small variations in the extremely slow percolation of the silica-bearing groundwater over time, possibly linked to changes in the background seismicity of the region, could determine minor fluctuations in the fluid composition, as indicated by discrete contrasts in fluid-inclusion salinity, and may have also contributed to shifts in the isotopic signatures of the calcite.

One advantage of this scenario is that it conciliates two contradictory observations regarding the mineralisation of the geodes. On the one hand, the transition from silica mineral crystallisation stages I and II seems to take place gradually and repeatedly, as observed in numerous samples from the present study (Fig. 4c, d, f). A progressive transition between chalcedony, quartz and amethyst has also been demonstrated by crystal size distribution of the mineralisation sequence in geodes in southern Brazil (Commin-Fischer et al. 2010). On the other hand, minerals from crystallisation stages I and II show contrasting isotopic compositions. Both observations can be satisfied in a scenario involving gradual changes in the isotopic composition of a single fluid with higher or lower water–rock interaction and in a context of alternating open and closed-systems related to an episodical recharge of groundwater into the geodes (Fig. 13c), without the need of a radically distinct fluid source.

The process and evolution of mineral crystallisation from a groundwater-like fluid is still a matter of debate. Direct crystallisation of quartz from hydrothermal fluids has been described in the literature (e.g., Williams and Crerar 1985;

Fournier 1989; Dong et al. 1995), but the volumetric constraints imposed by the geodes seems not to be compatible with this scenario. The solubility in water of various forms of silica (amorphous silica, opal, cristobalite, chalcedony and quartz) increases with temperature and is in the range of 10 to 100 mg $L^{-1}$ for temperatures of < 50–100 °C (Williams and Crerar 1985; Fournier 1989). Modelling with PhreeqC using the minteq.v4.dat database (U.S. Geological Survey) indicates that amorphous silica could dissolve to a Si concentration of 190 mg $L^{-1}$ at 100 °C in these waters. Considering the concentration of dissolved Si of 23.24 mg $L^{-1}$ in the analysed groundwater samples, which agrees with present-day silica-saturated compositions reported from the Guarani Aquifer by Arújo et al. (1999) and Morteani et al. (2010), as well as a limiting factor of $SiO_2$ precipitation of 7 mg $L^{-1}$ and a specific density of 2.65 g/cc for quartz, each cubic centimetre of quartz would require at least 163 L of water, which are orders of magnitude larger than the relative proportion between the volumes of the geodes and the mineralisation hosted in them. These calculations are based on practically neutral pH conditions of the groundwater. However, an increase of the pH, e.g., due to water circulation through the basalt and/or weathering processes, a higher amount of Si could be dissolved, leading to an enrichment of Si in the fluid. Later on, if this fluid is mixed with more acidic groundwater, $SiO_2$ precipitation would be induced due to the pH dependence of Si solubility. This scenario would require a smaller amount of fluid in order to precipitate the minerals, and could thereby contribute to silical-gel formation. Another possible scenario would be the mixing of a hydrothermal fluid (with higher Si solubility due to higher temperatures) with more acidic groundwater, leading to $SiO_2$ precipitation during cooling. Optimal conditions for silica precipitation are given for pH of 7 at 40 °C (Setiawan et al. 2019). The presence of amorphous silica (opal-A) and cryptocrystalline silica (chalcedony) suggests fast cooling due to the contact of the fluid and the cooled host rock, requiring a highly supersaturated gel-like silica fluid from which chalcedony directly precipitate (e.g., Götze et al. 2020 and references therein). In this case, a progressive decrease of the $SiO_2$ supersaturation of the fluid might result in a decrease of the number of quartz nuclei in the cryptocrystalline quartz, leading to a competitive growth that would result in the coarse-grained quartz that characterises the transition from crystallisation stage I to II. The repetition of chalcedony and coarse-grained quartz mineralisation at stage I that can be recognized in some of the geodes (Fig. 2e) would indicate a second infiltration of a highly supersaturated gel-like solution. However, it is not yet clear how this silica-rich gel forms.

Nevertheless, it is evident that the large quantity of coarse-grained quartz and amethyst likely requires large quantities of fluid to crystallise the volumes of silica minerals from a mineralising fluid with a composition close to groundwater. This implies the recurrent infiltration of slightly supersaturated fluid over a long-time span. Geochronological data, presently restricted to a few $^{40}Ar/^{39}Ar$ ages reported for celadonite samples from the rim and the core (celadonite inclusions in amethyst crystals) of geodes in Brazil, cover a large time period, ranging from 90 to 65 Ma (Vasconcelos 1998). This is in accordance with the model proposed here of a long-term process controlled by the low permeability of the host rock and a very slow infiltration rate, likely occurring over a period of millions of years.

From a geological point of view, a model in which all the minerals crystallise from groundwater-like fluids has the advantage of requiring no significant differences in the regional conditions in comparison to what is observed nowadays in the region. This is in accordance with the relative geological stability of the region, for which no major tectonic events are recorded after the extrusion of the basalts at ca. 135 Ma, and the subsequent opening of the South Atlantic Ocean (Hueck et al. 2017, 2019; Machado et al. 2020, 2021). Thus, the model proposed here for the amethyst mineralisation is consistent with the geological framework, and does not require a complex multi-event genesis, as proposed in previous contributions (e.g., Duarte et al. 2009, 2011; Hartmann et al. 2012a, b).

## Conclusions

In light of the new data and the novel methodology applied in this paper, we address some of the main questions regarding the genesis of the Los Catalanes amethyst deposits. The temperature conditions of the mineralisation and the origin and source of the mineralising fluid are determined by the application of state-of-the-art analytical methods in one-phase fluid inclusion nucleation-assisted microthermometry and triple-oxygen-isotope geochemistry. The new data confirm previous models that the mineralisation is related to a secondary process, which took place after the emplacement of the complete basalt pile being independent of magma crystallisation, as indicated by the coincidence of the fluid-inclusion and isotope data in the three mineralised lava flows. The high resolution provided by the one-phase fluid-inclusion microthermometry, combined with the reduced uncertainty in the isotopic signatures modelling provided by the triple-oxygen-isotope method, allows us to estimate with high confidence the temperature and composition of the mineralising fluid and compare it with geode-hosted water, strongly supporting previous models that the mineralisation is compatible with crystallisation from groundwater-like fluids. Low temperatures for the amethyst mineralisation between 15 and 60 °C are estimated for the first time in Uruguay.

The mineralising fluid has isotopic signatures of meteoric water, and low salinities from pure water up to 3% NaCl-eq., probably originating from the groundwater hosted in the underlying aquifers. In addition, deuterium isotopes, hydrogeochemistry from geode-hosted water and groundwater, and application of silica geothermometers also support a meteoric origin for the mineralising fluid and low-temperature conditions. We propose a simple model for the mineralisation process, in accordance with the regional geology. The model is based on the crystallisation of the different mineral phases inside pre-existing cavities, controlled by the low permeability of the host basalts and low infiltration rates over time. Interaction between the groundwater and the underlying units of the Paraná Basin under normal geothermal gradients, as well as with the host rock, accounts for the amethyst mineralisation. Episodic variations in the water flux during recurrent recharge of the mineralising fluids inside the geodes leads to different crystallisation phases.

**Supplementary Information** The online version contains supplementary material available at https://doi.org/10.1007/s00126-024-01310-2.

**Acknowledgements** F. Arduin Rode thanks Deutscher Akademischer Austauschdienst (DAAD) for the PhD scholarship (Forschungsstipendien – Promotionen in Deutschland, 2021/23—57552340) and Dirección Nacional de Minería y Geología, Ministerio de Industria, Energía y Minería of Uruguay (DINAMIGE-MIEM) for the support during the field trips and throughout the research project. The project was designated of ministerial interest by ministerial resolution (Res. 35/21) of the Ministerio de Industria Energía y Minería of Uruguay. Mining companies in Los Catalanes, Artigas are thanked for their consistent support in the geological surveys in the mines, their openness to collaborate with the research, and for donating all the samples used in the PhD. Harald Tonn and Axel Hackmann are highly acknowledged for their assistance with sample preparation. Petra Voigt, Anja Södje and Dr. Jago Birk from the Labor der Physischen Geographie, Geographisches Institut of the Georg-August-Universität Göttingen, are also highly acknowledged for providing the hydrogeochemical analyses of the water samples. Hernan Silva Lara is thanked for his support during the project, especially during one of the field campaigns in 2022. Finally, we would like to express our sincere gratitude to the anonymous reviewers and Associate Editor A. R. Cabral for their insightful and positive comments and suggestions, which have led to constructive discussions and significantly improved the quality of the manuscript.

**Author contribution** Intellectual work and conceptualization: Fiorella Arduin Rode.

Supervision: Graciela Sosa, Alfons van den Kerkhof, Pedro Oyhantçabal, Yves Krüger, David Bajnai, Klaus Wemmer, Mathias Hueck.

Field work: Fiorella Arduin Rode, Pedro Oyhantçabal, Klaus Wemmer, Graciela Sosa, Alfons van den Kerkhof, Siegfried Siegesmund.

Methodology: Fiorella Arduin Rode, Graciela Sosa, Alfons van den Kerkhof, Yves Krüger, David Bajnai, Andreas Pack, Klaus Wemmer, Tommaso Di Rocco, Daniel Herwartz, Swea Klipsch, Bettina Wiegand.

**Funding** Open Access funding enabled and organized by Projekt DEAL. Fiorella Arduin Rode is funded by a research grant in the frame of the doctoral program 2021/22—57552340 in Germany by the Deutscher Akademischer Austauschdienst (DAAD).

## Declarations

**Conflict of interest** The authors declare no competing interests.



## References

Apps JA (1983) Hydrothermal evolution of repository groundwaters in basalt. In: NRC nuclear waste geochemistry '83 : held at United States Geological Survey National Center, Reston, Virginia, August 30–31, 1983. NUREG/CP-0052

Arnuk WD, Guillerm E, Lowenstein TK et al (2024) Nucleation-assisted microthermometry: A novel application to fluid inclusions in halite. Chem Geol 122318. https://doi.org/10.1016/j.chemgeo.2024.122318

Aron PG, Levin NE, Beverly EJ et al (2021) Triple oxygen isotopes in the water cycle. Chem Geol 565:116770. https://doi.org/10.1016/j.chemgeo.2020.120026

Arújo LM, França AB, Potter PE (1999) Hydrogeology of the Mercosul aquifer system in the Paraná and Chaco-Paraná Basins, South America, and comparison with the Navajo-Nugget aquifer system, USA. Hydrogeol J 7:317–336. https://doi.org/10.1007/s100400050205

Bajnai D, Pack A, Arduin Rode F et al (2023) A dual inlet system for laser spectroscopy of triple oxygen isotopes in carbonate-derived and air $CO_2$. Geochem Geophys Geosyst 24:e2023GC010976. https://doi.org/10.1029/2023GC010976

Bajnai D, Cao X, Klipsch S et al (2024) Triple oxygen isotope systematics of $CO_2$ hydroxylation. Chem Geol 654:122059. https://doi.org/10.1016/j.chemgeo.2024.122059

Baker L, Franchi IA, Maynard J et al (2002) A technique for the determination of $^{18}O/^{16}O$ and $^{17}O/^{16}O$ isotopic ratios in water from small liquid and solid samples. Anal Chem 74:1665–1673. https://doi.org/10.1021/ac010509s

Barkan E, Luz B (2005) High precision measurements of $^{17}O/^{16}O$ and $^{18}O/^{16}O$ ratios in $H_2O$. Rapid Commun Mass Spectr 19:3737–3742. https://doi.org/10.1002/rcm.2250

Baumann N (2017) Historia de la minería en el Uruguay a comienzo del siglo XX (1903–1930): Una historia poco conocida, 1o edición. Jolly Roger Casa Editorial, Montevideo

Bellieni G, Comin-Chiaramonti P, Marques LS et al (1984) High- and low-$TiO_2$ flood basalts from the Paraná plateau (Brazil): Petrology and geochemical aspects bearing on their mantle origin. Neues Jahrbuch Miner Abh 140:273–306

Bodnar RJ (2003) Introduction to aqueous electrolyte fluid inclusions. In: Samson I, Anderson A, Marshall D (eds) Fluid Inclusions, Analysis and Interpretation. Mineralogical Association of Canada, pp 81–100

Chipera SJ, Apps JA (2001) Geochemical stability of natural zeolites. Rev Mineral Geochem 45:117–161. https://doi.org/10.2138/rmg.2001.45.3

Commin-Fischer A, Berger G, Polvé M et al (2010) Petrography and chemistry of $SiO_2$ filling phases in the amethyst geodes from the Serra Geral Formation deposit, Rio Grande do Sul, Brazil. J South Am Earth Sci 29:751–760. https://doi.org/10.1016/j.jsames.2009.10.002

Cordani UG, Vandoros P (1967) Basaltic rocks of the Paraná basin. In: Bigarella JJ, Becker RD, Pinto ID (eds) Problems in Brazilian Gondwana Geology

Corrêa TE, Koppe JC, Costa JFCL, Moraes MAL (1994) Caracterização geológica e critérios de prospecção de depósitos de ametista tipo "Alto Uruguai", RS. In: 38° Congresso Brasileiro de Geologia. Camboriú, Brasil

Craig H (1961) Isotopic variations in meteoric waters. Science 133:1702–1703. https://doi.org/10.1126/science.133.3465.1702

Da Silva JS (1997) Geografía de las ágatas y amatistas del Uruguay. In: Da Silva JS (ed) GeoUruguay. pp 83–100

Daëron M, Drysdale RN, Peral M et al (2019) Most Earth-surface calcites precipitate out of isotopic equilibrium. Nat Commun 10:429. https://doi.org/10.1038/s41467-019-08336-5

de Brito Neves BB, Fuck RA (2013) Neoproterozoic evolution of the basement of the South-American platform. J South Am Earth Sci 47:72–89. https://doi.org/10.1016/j.jsames.2013.04.005

de Assis JV, de Freitas VA, Heaman LH (2011) The onset of flood basalt volcanism, Northern Paraná Basin, Brazil: A precise U-Pb baddeleyite/zircon age for a Chapecó-type dacite. Earth Planet Sci Lett 302:147–153. https://doi.org/10.1016/j.epsl.2010.12.005

Dong G, Morrison G, Jaireth S (1995) Quartz textures in epithermal veins, Queensland; classification, origin and implication. Econ Geol 90:1841–1856. https://doi.org/10.2113/gsecongeo.90.6.1841

Duarte LC, Hartmann LA, Vasconcellos MAZ et al (2009) Epigenetic formation of amethyst-bearing geodes from Los Catalanes gemological district, Artigas, Uruguay, southern Paraná Magmatic Province. J Volcanol Geotherm Res 184:427–436. https://doi.org/10.1016/j.jvolgeores.2009.05.019

Duarte LC, Hartmann LA, Ronchi LH et al (2011) Stable isotope and mineralogical investigation of the genesis of amethyst geodes in the Los Catalanes gemological district, Uruguay, southernmost Paraná volcanic province. Miner Deposita 46:239–255. https://doi.org/10.1007/s00126-010-0323-6

Duplay J, Paquet H, Kossovskaya A, Tard Y (1989) Estimation de la température de formation des paragenèses saponite-céladonite et glauconite–nontronite dans les altérations sous-marines de basalte, par la méthode des corrélations entre éléments au sein de populations monominérales. C R Acad Sci Paris Série II 309:53–58

Florisbal LM, Heaman LM, de Assis JV, de Fatima BM (2014) Tectonic significance of the Florianópolis Dyke Swarm, Paraná-Etendeka Magmatic Province: A reappraisal based on precise U-Pb dating. J Volcanol Geotherm Res 289:140–150. https://doi.org/10.1016/j.jvolgeores.2014.11.007

Fournier RO (1977) Chemical geothermometers and mixing models for geothermal systems. Geothermics 5:41–50. https://doi.org/10.1016/0375-6505(77)90007-4

Fournier RO (1989) Geochemistry and dynamics of the Yellowstone National Park hydrothermal system. Annu Rev Earth Planet Sci 17:13–53. https://doi.org/10.1146/annurev.ea.17.050189.000305

Frank HT, Gomes MEB, Formoso MLL (2009) Review of the areal extent and the volume of the Serra Geral Formation Paraná Basin South America. Pesqui Geociênc 36:49–57

Gilg HA, Morteani G, Kostitsyn Y et al (2003) Genesis of amethyst geodes in basaltic rocks of the Serra Geral Formation (Ametista do Sul, Rio Grande do Sul, Brazil): a fluid inclusion, REE, oxygen, carbon, and Sr isotope study on basalt, quartz, and calcite. Miner Deposita 38:1009–1025. https://doi.org/10.1007/s00126-002-0310-7

Gilg HA, Krüger Y, Taubald H et al (2014) Mineralisation of amethyst-bearing geodes in Ametista do Sul (Brazil) from low-temperature sedimentary brines: evidence from monophase liquid inclusions and stable isotopes. Miner Deposita 49:861–877. https://doi.org/10.1007/s00126-014-0522-7

Gomes MEB (1996) Mecanismos de resfriamento estruturação e processos pós-magmáticos em basaltos da Bacia do Paraná: Região de Frederico Westphalen (RS)-Brasil. Universidade Federal do Rio Grande do Sul, PhD

Götze J, Möckel R, Vennemann T, Müller A (2016) Origin and geochemistry of agates in Permian volcanic rocks of the Sub-Erzgebirge basin, Saxony (Germany). Chem Geol 428:77–91. https://doi.org/10.1016/j.chemgeo.2016.02.023

Götze J, Möckel R, Pan Y (2020) Mineralogy, geochemistry and genesis of agate—a review. Minerals 10:1037. https://doi.org/10.3390/min10111037

Guerrero S, Morales Demarco M (2019) Génesis de los yacimientos de ágatas y amatistas en el "Distrito gemológico Los Catalanes": revisión de antecedentes y observaciones de campo. In: IX Congreso Uruguayo de Geología. Trinidad Flores, Uruguay

Guo W, Zhou C (2019) Triple oxygen isotope fractionation in the DIC-$H_2O$-$CO_2$ system: A numerical framework and its implications. Geochim Cosmochim Acta 246:541–564. https://doi.org/10.1016/j.gca.2018.11.018

Hamdan I, Wiegand B, Toll M, Sauter M (2016) Spring response to precipitation events using $\delta^{18}O$ and $\delta^{2}H$ in the Tanour catchment, NW Jordan. Isot Environ Health Stud 52:682–693. https://doi.org/10.1080/10256016.2016.1159205

Hartmann LA, Wildner W, Duarte LC et al (2010) Geochemical and scintillometric characterization and correlation of amethyst geode-bearing Paraná lavas from the Quaraí and Los Catalanes districts, Brazil and Uruguay. Geol Mag 147:954–970. https://doi.org/10.1017/S0016756810000592

Hartmann LA, Da Cunha DL, Massonne H-J et al (2012a) Sequential opening and filling of cavities forming vesicles, amygdales and giant amethyst geodes in lavas from the southern Paraná volcanic province, Brazil and Uruguay. Int Geol Rev 54:1–14. https://doi.org/10.1080/00206814.2010.496253

Hartmann LA, Medeiros JTN, Petruzzellis LT (2012b) Numerical simulations of amethyst geode cavity formation by ballooning of altered Paraná volcanic rocks, South America. Geofluids 12:133–141. https://doi.org/10.1111/j.1468-8123.2011.00346.x

Hartmann LA, Antunes LM, Rosenstengel LM (2014) Stratigraphy of amethyst geode-bearing lavas and fault-block structures of the Entre Rios mining district, Paraná volcanic province, southern Brazil. An Acad Bras Ciênc 86:187–198. https://doi.org/10.1590/0001-37652014201120004

Herwartz D (2021) Triple oxygen isotope variations in Earth's crust. Rev Mineral Geochem 86:291–322. https://doi.org/10.2138/rmg.2021.86.09

Herwartz D, Surma J, Voigt C et al (2017) Triple oxygen isotope systematics of structurally bonded water in gypsum. Geochim Cosmochim Acta 209:254–266. https://doi.org/10.1016/j.gca.2017.04.026

Hilario A, Asrat A, van Wyk de Vries B, Mogk D, Lozano Otero G, Zhang J, Brilha J, Vegas J, Lemon K, Carcavilla L, Finney S (2022) The first 100 IUGS geological heritage sites. International Union of Geological Sciences

Holdsworth CM, John CM, Snæbjörnsdóttir SÓ et al (2024) Reconstructing the temperature and origin of $CO_2$ mineralisation in CarbFix calcite using clumped, carbon and oxygen isotopes.

Appl Geochem 162:105925. https://doi.org/10.1016/j.apgeochem.2024.105925
Holz M, Küchle J, Philipp RP et al (2006) Hierarchy of tectonic control on stratigraphic signatures: Base-level changes during the Early Permian in the Paraná Basin, southernmost Brazil. J South Am Earth Sci 22:185–204. https://doi.org/10.1016/j.jsames.2006.09.007
Hueck M, Oriolo S, Dunkl I et al (2017) Phanerozoic low-temperature evolution of the Uruguayan Shield along the South American passive margin. J Geol Soc 174:609–626. https://doi.org/10.1144/jgs2016-101
Hueck M, Dunkl I, Oriolo S et al (2019) Comparing contiguous high- and low-elevation continental margins: New (U-Th)/He constraints from South Brazil and an integration of the thermochronological record of the southeastern passive margin of South America. Tectonophysics 770:228222. https://doi.org/10.1016/j.tecto.2019.228222
Hueck M, Wemmer K, Basei MAS et al (2020) Dating recurrent shear zone activity and the transition from ductile to brittle deformation: White mica geochronology applied to the Neoproterozoic Dom Feliciano Belt in South Brazil. J Struct Geol 141:104199. https://doi.org/10.1016/j.jsg.2020.104199
Hueck M, Oriolo S, Basei MAS et al (2022) Archean to early Neoproterozoic crustal growth of the southern South American Platform and its wide-reaching "African" origins. Precamb Res 369:106532. https://doi.org/10.1016/j.precamres.2021.106532
Iler RK (1979) The chemistry of silica, solubility, polymerization, colloid and surface properties, and biochemistry. p 866
Juchem PL (1999) Mineralogia, Geologia e Gênese dos Depósitos de Ametista da Região do Alto Uruguai. Doutorado em Mineralogia e Petrologia, Universidade de São Paulo, Rio Grande do Sul
Koltai G, Kluge T, Krüger Y et al (2024) Geothermometry of calcite spar at 10–50 °C. Sci Rep 14:1553. https://doi.org/10.1038/s41598-024-71856-7
Krüger Y, Stoller P, Rička J, Frenz M (2007) Femtosecond lasers in fluid-inclusion analysis: overcoming metastable phase states. Eur J Mineral 19:693–706. https://doi.org/10.1127/0935-1221/2007/0019-1762
Krüger Y, Marti D, Staub RH et al (2011) Liquid–vapour homogenisation of fluid inclusions in stalagmites: Evaluation of a new thermometer for palaeoclimate research. Chem Geol 289:39–47. https://doi.org/10.1016/j.chemgeo.2011.07.001
Krüger Y, García-Ruiz JM, Canals À et al (2013) Determining gypsum growth temperatures using monophase fluid inclusions—Application to the giant gypsum crystals of Naica, Mexico. Geology 41:119–122. https://doi.org/10.1130/G33573.1
Leinz V (1949) Contribuição à Geologia dos Derrames Basálticos do Sul do Brasil. Bol Fac Filos Ciênc Let Univ São Paulo. Geol 1. https://doi.org/10.11606/issn.2526-3862.bffcluspgeologia.1949.121703
Løland MH, Krüger Y, Fernandez A et al (2022) Evolution of tropical land temperature across the last glacial termination. Nat Commun 13:5158. https://doi.org/10.1038/s41467-022-32853-x
Luz B, Barkan E (2010) Variations of $^{17}O/^{16}O$ and $^{18}O/^{16}O$ in meteoric waters. Geochim Cosmochim Acta 74:6276–6286. https://doi.org/10.1016/j.gca.2010.08.016
Machado JPSL, Ritter Jelinek A, Stephenson R et al (2020) Low-temperature thermochronology of the South Atlantic margin along Uruguay and its relation to tectonic events in West Gondwana. Tectonophysics 784:228439. https://doi.org/10.1016/j.tecto.2020.228439
Machado JP, Jelinek AR, Stephenson R, O'Sullivan P (2021) Thermochronology of South America passive margin between Uruguay and southern Brazil: A lengthy and complex cooling history based on (U–Th)/He and fission tracks. J South Am Earth Sci 106:103019. https://doi.org/10.1016/j.jsames.2020.103019
Mantovani MSM, Marques LS, De Sousa MA et al (1985) Trace element and strontium isotope constraints on the origin and evolution of Paran Continental Flood Basalts of Santa Catarina State (Southern Brazil). J Petrol 26:187–209. https://doi.org/10.1093/petrology/26.1.187
Marti D, Krüger Y, Fleitmann D et al (2012) The effect of surface tension on liquid–gas equilibria in isochoric systems and its application to fluid inclusions. Fluid Phase Equilib 314:13–21. https://doi.org/10.1016/j.fluid.2011.08.010
Marti D, Krüger Y, Frenz M (2009) Fluid inclusion liquid-vapour homogenization in the vicinity of the density maximum of aqueous solutions. In: ECROFI XX European Current Research on Fluid Inclusions. Granada, Spain
Matsui E, Salati E, Marini OJ (1974) D/H and $^{18}O/^{16}O$ ratios in waters contained in geodes from the basaltic province of Rio Grande do Sul. Brazil Geol Soc America Bull 85:577. https://doi.org/10.1130/0016-7606(1974)85%3c577:DAORIW%3e2.0.CO;2
McCrea JM (1950) On the Isotopic Chemistry of Carbonates and a Paleotemperature Scale. J Chem Phys 18:849–857. https://doi.org/10.1063/1.1747785
Morales E, Veroslavsky G, Manganelli A et al (2021) Potential of geothermal energy in the onshore sedimentary basins of Uruguay. Geothermics 95:102165. https://doi.org/10.1016/j.geothermics.2021.102165
Morteani G, Kostitsyn Y, Preinfalk C, Gilg HA (2010) The genesis of the amethyst geodes at Artigas (Uruguay) and the paleohydrology of the Guaraní aquifer: structural, geochemical, oxygen, carbon, strontium isotope and fluid inclusion study. Int J Earth Sci 99:927–947. https://doi.org/10.1007/s00531-009-0439-z
Neuser RD, Bruhn F, Götze J et al (1995) Kathodolumineszenz: Methodik und Anwendung. Zbl Geol Paläont Teil I 1:287–306
Oyhantçabal P, Siegesmund S, Wemmer K (2011) The Río de la Plata Craton: a review of units, boundaries, ages and isotopic signature. Int J Earth Sci 100:201–220. https://doi.org/10.1007/s00531-010-0580-8
Oyhantçabal P, Cingolani CA, Wemmer K, Siegesmund S (2018) The Río de la Plata Craton of Argentina and Uruguay. In: Siegesmund S, Basei MAS, Oyhantçabal P, Oriolo S (eds) Geology of Southwest Gondwana. Springer, pp 89–105
Pack A (2021) Isotopic traces of atmospheric $O_2$ in rocks, minerals, and melts. Rev Mineral Geochem 86:217–240. https://doi.org/10.2138/rmg.2021.86.07
Pack A, Herwartz D (2014) The triple oxygen isotope composition of the Earth mantle and understanding $\Delta^{17}O$ variations in terrestrial rocks and minerals. Earth Planet Sci Lett 390:138–145. https://doi.org/10.1016/j.epsl.2014.01.017
Pack A, Tanaka R, Hering M et al (2016) The oxygen isotope composition of San Carlos olivine on the VSMOW2-SLAP2 scale. Rapid Commun Mass Spectr 30:1495–1504. https://doi.org/10.1002/rcm.7582
Pasqualetto L, Krüger Y, Meckler AN (2023) Microthermometry on fluid inclusions in stalagmites: what does the retrograde homogenisation tell us? In: ECROFI XXIII European Current Research on Fluid Inclusions. Reykjavik, Iceland
Peate DW (1997) The Paraná-Etendeka Province. In: Mahoney JJ, Coffin MF (eds) Large Igneous Provinces: Continental, Oceanic, and Planetary Flood Volcanism. American Geophysical Union, Washington, D. C., pp 217–245
Peate DW, Hawkesworth CJ, Mantovani MSM (1992) Chemical stratigraphy of the Paraná lavas (South America): Classification of magma types and their spatial distribution. Bull Volcanol 55:119–139. https://doi.org/10.1007/BF00301125
Peters STM, Alibabaie N, Pack A et al (2020) Triple oxygen isotope variations in magnetite from iron-oxide deposits, central Iran,

record magmatic fluid interaction with evaporite and carbonate host rocks. Geology 48:211–215. https://doi.org/10.1130/G46981.1

Proust D, Fontaine C (2007a) Amethyst-bearing lava flows in the Paraná Basin (Rio Grande do Sul, Brazil): cooling, vesiculation and formation of the geodic cavities. Geol Mag 144:53–65. https://doi.org/10.1017/S001675680600269X

Proust D, Fontaine C (2007b) Amethyst geodes in the basaltic flow from Triz quarry at Ametista do Sul (Rio Grande do Sul, Brazil): magmatic source of silica for the amethyst crystallisations. Geol Mag 144:731–739. https://doi.org/10.1017/S0016756807003457

Qiu C, Krüger Y, Wilke M et al (2016) Exploration of the phase diagram of liquid water in the low-temperature metastable region using synthetic fluid inclusions. Phys Chem Chem Phys 18:28227–28241. https://doi.org/10.1039/C6CP04250C

Rocha BC, Davies JHFL, Janasi VA et al (2020) Rapid eruption of silicic magmas from the Paraná magmatic province (Brazil) did not trigger the Valanginian event. Geology 48:1174–1178. https://doi.org/10.1130/G47766.1

Rocha BC, Gaynor SP, Janasi VA et al (2023) New U-Pb baddeleyite ID-TIMS ages from the intrusive high-Ti-Sr rocks of the Southern Paraná LIP, Brazil: Implications for correlations with environmental disturbances during the Early Cretaceous. Res Geochem 10:100023. https://doi.org/10.1016/j.ringeo.2023.100023

Roedder E (1984) Fluid inclusions: an introduction to studies of all types of fluid inclusions, gas, liquid, or melt, trapped in materials from earth and space, and their application to the understanding of geologic processes. Mineralogical Soc. of America, Blacksburg, Va

Rossetti L, Lima EF, Waichel BL et al (2018) Lithostratigraphy and volcanology of the Serra Geral Group, Paraná-Etendeka Igneous Province in Southern Brazil: Towards a formal stratigraphical framework. J Volcanol Geotherm Res 355:98–114. https://doi.org/10.1016/j.jvolgeores.2017.05.008

Rostirola SP, Assine ML, Fernandes LA, Artur PC (2000) Reativação de paleolineamentos durante a evolução da bacia do Paraná - o exemplo do alto estrutural de quatinguá. Rev Bras Geociênc 30:639–648. https://doi.org/10.25249/0375-7536.2000304639648

Schoenemann SW, Schauer AJ, Steig EJ (2013) Measurement of SLAP2 and GISP $\delta^{17}O$ and proposed VSMOW-SLAP normalization for $\delta^{17}O$ and $^{17}O_{excess}$. Rapid Commun Mass Spectr 27:582–590. https://doi.org/10.1002/rcm.6486

Scopel RM, Gomes MEB, Formoso MLL, Proust D (1998) Derrames portadores de ametistas na região de Frederico Westphalen-Irai-Planalto-Ametista do Sul RS-Brasil. In: II Congreso Uruguayo de Geología. Punta del Este, pp 243–248

Setiawan FA, Rahayuningsih E, Petrus HTBM et al (2019) Kinetics of silica precipitation in geothermal brine with seeds addition: minimizing silica scaling in a cold re-injection system. Geotherm Energy 7:22. https://doi.org/10.1186/s40517-019-0138-3

Sharp ZD (1990) A laser-based microanalytical method for the in situ determination of oxygen isotope ratios of silicates and oxides. Geochim Cosmochim Acta 54:1353–1357. https://doi.org/10.1016/0016-7037(90)90160-m

Sharp ZD, Gibbons JA, Maltsev O et al (2016) A calibration of the triple oxygen isotope fractionation in the $SiO_2$–$H_2O$ system and applications to natural samples. Geochim Cosmochim Acta 186:105–119. https://doi.org/10.1016/j.gca.2016.04.047

Shepherd TJ (1981) Temperature-programmable, heating-freezing stage for microthermometric analysis of fluid inclusions. Econ Geol 76:1244–1247. https://doi.org/10.2113/gsecongeo.76.5.1244

Sparks RSJ (1978) The dynamics of bubble formation and growth in magmas: A review and analysis. J Volcanol Geotherm Res 3:1–37. https://doi.org/10.1016/0377-0273(78)90002-1

Strugale M, Rostirolla SP, Mancini F et al (2007) Structural framework and Mesozoic-Cenozoic evolution of Ponta Grossa Arch, Paraná Basin, southern Brazil. J South Am Earth Sci 24:203–227. https://doi.org/10.1016/j.jsames.2007.05.003

Surma J, Assonov S, Bolourchi MJ, Staubwasser M (2015) Triple oxygen isotope signatures in evaporated water bodies from the Sistan Oasis. Iran Geophys Res Lett 42:8456–8462. https://doi.org/10.1002/2015gl066475

Techera J, Loureiro J, Spoturno J (2007) Cartografía geológica y relevamiento minero en el Distrito Gemológico Los Catalanes Artigas – Uruguay, Proyecto Agatas Y Amatistas Fase I. Montevideo

van den Kerkhof AM, Hein UF (2001) Fluid inclusion petrography. Lithos 55:27–47. https://doi.org/10.1016/S0024-4937(00)00037-2

Vasconcelos PM (1998) $^{40}Ar/^{39}Ar$ dating of celadonite and the formation of amethyst geodes in the Paraná Continental Flood Basalt Province. In: AGU. San Francisco, USA

Veroslavsky G, Rossello EA, López-Gamundí O et al (2021) Late Paleozoic tectono-sedimentary evolution of eastern Chaco-Paraná Basin (Uruguay, Brazil, Argentina and Paraguay). J South Am Earth Sci 106:102991. https://doi.org/10.1016/j.jsames.2020.102991

Wagner W, Pruß A (2002) The IAPWS formulation 1995 for the thermodynamic properties of ordinary water substance for general and scientific use. J Phys Chem Ref Data 31:387–535. https://doi.org/10.1063/1.1461829

Whitney DL, Evans BW (2010) Abbreviations for names of rock-forming minerals. Am Miner 95:185–187. https://doi.org/10.2138/am.2010.3371

Williams LA, Crerar DA (1985) Silica diagenesis; II, General mechanisms. J Sediment Res 55:312–321. https://doi.org/10.1306/212F86B1-2B24-11D7-8648000102C1865D

Williams LA, Parks GA, Crerar DA (1985) Silica diagenesis; I, solubility controls. J Sediment Res 55(3):301–311. https://doi.org/10.1306/212f86ac-2b24-11d7-8648000102c1865d

Wostbrock JAG, Sharp ZD, Sanchez-Yanez C et al (2018) Calibration and application of silica-water triple oxygen isotope thermometry to geothermal systems in Iceland and Chile. Geochim Cosmochim Acta 234:84–97. https://doi.org/10.1016/j.gca.2018.05.007

Wostbrock JAG, Brand U, Coplen TB et al (2020a) Calibration of carbonate-water triple oxygen isotope fractionation: Seeing through diagenesis in ancient carbonates. Geochim Cosmochim Acta 288:369–388. https://doi.org/10.1016/j.gca.2020.07.045

Wostbrock JAG, Cano EJ, Sharp ZD (2020b) An internally consistent triple oxygen isotope calibration of standards for silicates, carbonates and air relative to VSMOW2 and SLAP2. Chem Geol 533:119432. https://doi.org/10.1016/j.chemgeo.2019.119432

Zakharov DO, Bindeman IN, Tanaka R et al (2019) Triple oxygen isotope systematics as a tracer of fluids in the crust: A study from modern geothermal systems of Iceland. Chem Geol 530:119312. https://doi.org/10.1016/j.chemgeo.2019.119312

Zalán PV, Wolff S, Astolfi MAM, et al (1990) The Parana Basin, Brazil: Chapter 33: Part II. Selected Analog Interior Cratonic Basins: Analog Basins. In: Leighton MW, Kolata DR, Oltz DF, Eidel JJ (eds) AAPG Memoirs 51: Interior Cratonic Basins. pp 681–708